RF PULSE DESIGN FOR PARALLEL EXCITATION IN MAGNETIC RESONANCE IMAGING

A Dissertation

by

YINAN LIU

Submitted to the Office of Graduate Studies of
Texas A&M University
in partial fulfillment of the requirements for the degree of

DOCTOR OF PHILOSOPHY

May 2012

Major Subject: Electrical Engineering

RF Pulse Design for Parallel Excitation in Magnetic Resonance Imaging

RF PULSE DESIGN FOR PARALLEL EXCITATION IN MAGNETIC RESONANCE IMAGING

A Dissertation

by

YINAN LIU

Submitted to the Office of Graduate Studies of
Texas A&M University
in partial fulfillment of the requirements for the degree of

DOCTOR OF PHILOSOPHY

Approved by:

Chair of Committee,	Jim X. Ji
Committee Members,	Steven M. Wright
	Andrew Chan
	Mary McDougall
Head of Department,	Costas N. Georghiades

May 2012

Major Subject: Electrical Engineering

ABSTRACT

RF Pulse Design for Parallel Excitation in
Magnetic Resonance Imaging. (May 2012)
Yinan Liu, B.S., University of Science and Technology of China
Chair of Advisory Committee: Dr. Jim X. Ji

Parallel excitation is an emerging technique to improve or accelerate multi-dimensional spatially selective excitations in magnetic resonance imaging (MRI) using multi-channel transmit arrays. The technique has potential in many applications, such as accelerating imaging speed, mitigating field inhomogeneity in high-field MRI, and alleviating the susceptibility artifact in functional MRI (fMRI). In these applications, controlling radiofrequency (RF) power deposition (quantified by Specific Absorption Rate, or SAR) under safe limit is a critical issue, particularly in high-field MRI. This dissertation will start with a review of multidimensional spatially selective excitation in MRI and current parallel excitation techniques. Then it will present two new RF pulse design methods to achieve reduced local/global SAR for parallel excitation while preserving the time duration and excitation pattern quality. Simulations incorporating human-model based tissue density and dielectric property were performed. Results have show that the proposed methods can achieve significant SAR reductions without enlonging the pulse duration at high-fields.

NOMENCLATURE

AP	Artifact Power
CD	Constant Density
FOX	Field of Excitation
FOV	Field of View
M	Magnetization
MRI	Magnetic Resonance Imaging
RF	Radiofrequency
SAR	Specific Absorption Rate
VD	Variable Density

TABLE OF CONTENTS

Page

LIST OF FIGURES

Figure Page

1. INTRODUCTION

1.1 Problem Statement

Multidimensional spatially selective excitation using radiofrequency (RF) pulses in the presence of time-varying magnetic gradients (1) has wide applications particularly in high-field MRI, such as inner volume excitation, curved slice imaging and mitigating field inhomogeneity in high field (2-4). However, due to limitations in gradient hardware performance and RF power restriction, such pulse designs can result in long waveforms that may limit their performance and practical applicability. Recently, with the development of multi-channel transmit coil arrays that are capable of simultaneous, independent RF pulse transmission, parallel excitation can be achieved with shortened RF pulse durations by taking advantage of distinctions in transmit sensitivity profiles among coils (5-8).

Parallel excitation is a promising technique for high-field MRI. Unfortunately, elevated RF power deposition, or specific absorption rate (SAR) is a major concern before this technique could be applied in clinical applications. When multi-channel transmit arrays are simultaneously employed, the electric fields generated by each channel undergo local superposition and thus local extremes in electric field magnitude may arise (9), causing spikes in local SAR (“hot spots”). Reduce pulse duration using parallel excitation

---

This dissertation follows the style of Magnetic Resonance in Medicine.

would further lead to increased RF pulse power and thus increased global and peak SAR (10-11).

1.2 Dissertation Objective

The objective of this research is to develop two methods to reduce local/global SAR in parallel excitation while preserving the RF pulse duration and the excitation pattern quality. The first algorithm is based on adapting variable-density spiral trajectories. The second algorithm achieves reduced SAR by iteratively adjusting both RF pulses and k-space trajectories. A unique feature of this framework is that it incorporates tissue density and dielectric properties.

1.3 Dissertation Organization

The rest of the dissertation is organized as follows: Section 2 will introduce the basic principle of multidimensional spatially selective excitation; Section 3 will review current parallel excitation techniques and discuss in detail the elevated SAR problem associated with parallel excitation; Section 4 will describe the design of variable density spiral trajectory and its application to reduce SAR; Section 5 will present a design method for iteratively adjusting RF pulses and k-space trajectories for SAR reduction.

2. INTRODUCTION TO SPATIALLY SELECTIVE EXCITATION OF MAGNETIC RESONANCE IMAGING

Multidimensional spatially selective excitation (2-4,12-14) is a widely used technique in MRI to confine the signal-contributing volume to only the selected region. Slice-selective excitation is one of the most commonly used forms of spatially selective excitation, which limits the signal-contributing volume to a thin slice. Higher dimensional spatially excitations are also feasible, which allows performing imaging or spectroscopy within only an inner volume of a large object. Multidimensional spatially-selective excitation have been used in a wide range of MRI applications, such as inner volume excitation, outer volume suppression (12-13), curved slice imaging (4), localized spectroscopy (2-3), and reduced-FOV scan of a region of interest (13). Moreover, with the advancement of high-fields MRI, spatially selective excitation has gained great interest to compensate field inhomogeneity (15) and to reduce susceptibility artifacts (16). In multidimensional spatially selective excitation, radiofrequency (RF) pulses are combined with appropriate gradient waveforms for spatially selectivity. The performance of the gradient system is of critical importance for selective excitation. One distinct obstacle for selective excitation is the long RF pulse duration because of the imperfection of the gradient system or the gradient constrains. In this section, the principle of multidimensional spatially selective excitation is described.

2.1 Bloch Equation

MRI is based on the interaction of a nuclear spin with an external magnetic field $\vec{B}_0$. In the absence of external magnetic field, the dipoles of the nuclear spins randomly orient themselves to all directions. When the external magnetic field is applied, the spins will point in a direction parallel to $\vec{B}_0$, and will start to rotate about the axis parallel to $\vec{B}_0$ (Fig. 2.1).

The precession angular frequency for the proton magnetic moment vector is given by

$$\omega_0 = \gamma B_0 \tag{2.1}$$

where γ is the gyromagnetic ratio. For ^{1}H, $\gamma = 42.58$ MHz/Tesla.

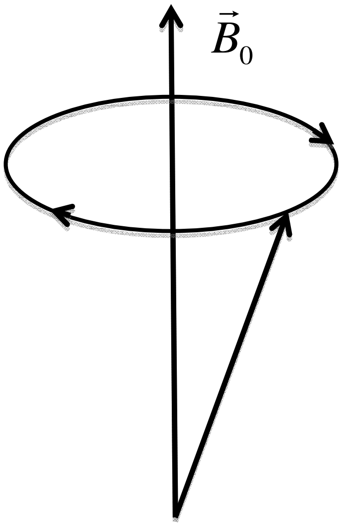

Figure 2.1. Precession of a nuclear spin about an external magnetic field.

The imaging of an object relies on the bulk precession of the hydrogen spins in water, fat and other organic molecules. When the object is placed in a static external magnetic field, where B_0 is applied in the z-direction of the laboratory frame, the bulk magnetization vector points along the positive direction of z-axis at equilibrium, creating a non-zero net magnetization:

$$M_0 = \frac{\gamma^2 h^2 N_s}{4KT_s} B_0 \tag{2.2}$$

where h is Planck's constant ($6.6\times10^{-34} J/s$), K is the Boltzmann constant ($1.38\times10^{-23} J/K$), T_s is the absolute temperature of the spin system, N_s is the number of spins.

To generate a detectable MRI signal, the equilibrium magnetization needs to be rotated away from its alignment along the $\vec{B}_0$ axis by applying oscillating radiofrequency (RF) pulses, $\vec{B}_1(t)$, for a short time (Fig.2.2). The RF pulses lie in the XY-plane (transverse plane). The rotating magnetization yield a changing flux in any nearby coil, which will result in a signal detectable by MRI scanner.

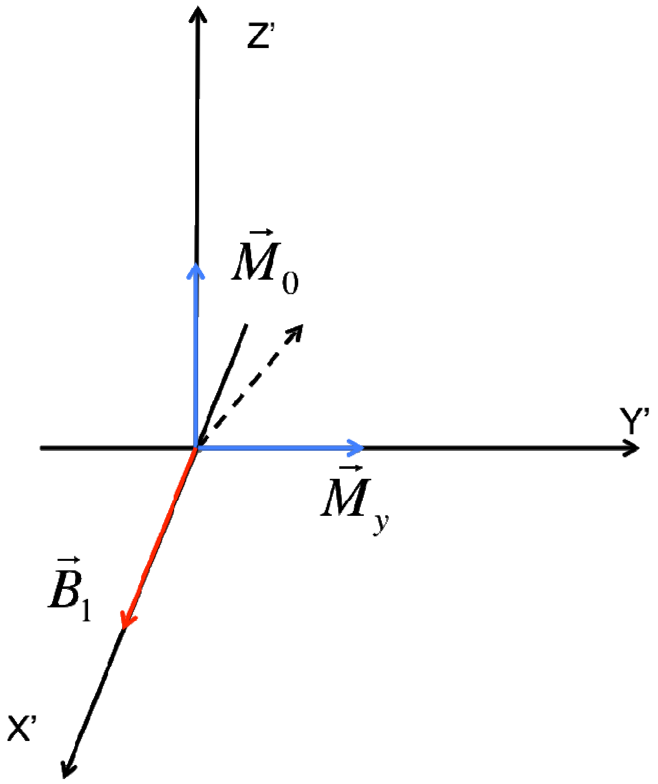

Figure 2.2. Illustration of the effect of a 90° RF pulse which rotates the equilibrium magnetization down to the Y' axis in a rotating frame.

In the presence of a time varying RF pulse $\vec{B}_1(t)$, the behavior of magnetization $\vec{M}$ is also time-dependent, which is described quantitatively by the Bloch equation.

$$\frac{d\vec{M}}{dt} = \gamma\vec{M} \times \vec{B}_1 + \frac{1}{T_1}\left(M_0 - M_z\right) - \frac{1}{T_2}\vec{M}_\perp \tag{2.3}$$

where $\vec{M}_\perp = M_x\hat{x} + M_y\hat{y}$ is the transverse magnetization component, T_1 is the spin-lattice relaxation time, T_2 is the spin-spin relaxation time. T_1 and T_2 vary as a function of magnetic field strength, and are used to describe the signal regrowth along longitudinal and signal decay along transverse direction respectively.

2.2 Spatially Selective Excitation

Spatially selective RF pulses are applied simultaneously with 3D oscillating gradient waveforms to achieve multidimensional spatially selectivity. In this case, the Bloch equation is difficult to solve. Pauly and colleagues have introduced a k-space analysis method to solve Bloch equation under small flip angle assumption (1). This k-space analysis method will be the foundations for parallel excitation techniques described later in Section 3. In this section, the k-space analysis of Bloch equation is reviewed.

The RF pulse is short lived, and when the duration is so small that the relaxation effect could be ignored, the Bloch equation (Eq.(2.3)) in the presence of gradients and an RF field becomes (1).

$$\frac{d\vec{M}}{dt} = \gamma\vec{M} \times \left(\vec{B}_1 + \left(\mathbf{G}\cdot\mathbf{r}\right)\vec{z}\right) \tag{2.4}$$

where $\mathbf{G} = \left(G_x, G_y, G_z\right)$ denotes the gradient waveform, $\mathbf{r} = \left(x, y, z\right)$ denotes the spatial position. When the RF is applied in the transverse plane, $\vec{B}_1 = \left(B_{1x}, B_{1y}, 0\right)$, Eq.(2.4) can be rewritten as

$$\begin{pmatrix} dM_x / dt \\ dM_y / dt \\ dM_z / dt \end{pmatrix} = \gamma \begin{pmatrix} 0 & \mathbf{G}\cdot\mathbf{r} & -B_{1,y} \\ -\mathbf{G}\cdot\mathbf{r} & 0 & B_{1,x} \\ B_{1y} & -B_{1x} & 0 \end{pmatrix} \begin{pmatrix} M_x \\ M_y \\ M_z \end{pmatrix} \tag{2.5}$$

Under the small flip angle assumption, if the flip angle θ is close to 0, $\cos\theta \approx 1$ and $M_z \approx M_0$, then Eq. (2.5) can be decoupled into transverse and longitudinal equations. The resulting equations for M_x and M_y can be combined by choosing

$$M_+ \equiv M_x + iM_y$$

and

$$B_1 \equiv B_{1x} + iB_{1y}$$

Then Eq. (2.5) reduces to

$$dM_+ / dt = -i\gamma\left(\mathbf{G}\cdot\mathbf{r}\right)M_+ + i\gamma B_1 M_0 \tag{2.6}$$

Assume that the duration of RF pulse $\vec{B}_1(t)$ is T, initial transverse magnetization $M_x(0) = M_y(0) = 0$, and initial longitudinal magnetization $M_z^0 = M_0$. Equation (2.6) can be integrated over the interval $(0,T)$ (1).

$$M_+(\mathbf{r},T) = i\gamma M_0 \int_0^T dt B_1(t) e^{i2\pi\mathbf{k}(t)\cdot\mathbf{r}} \tag{2.7}$$

where $\mathbf{k}(t)$ is a spatial frequency variable introduced to denote the integral of the remaining gradient area

$$\mathbf{k}(t) = -\gamma \int_t^T \mathbf{G}(\tau) d\tau \tag{2.8}$$

Equation (2.7) establishes a Fourier transform relationship between the transverse magnetization and the applied RF pulse. More particularly, it shows that RF pulse applies a weighting in k-space domain and the transverse magnetization is the Fourier transform of the applied RF pulse along a k-space trajectory determined by the gradient waveform. An example of slice-selective excitation is illustrated in Fig. 2.3. In this case, the gradient is a constant, and the rectangular slice profile is the Fourier Transform of the ideal sinc RF waveform. One thing to note is that, to achieve a well-defined rectangular slice, the ideal sinc RF pulse needs to have infinite pulse duration, which is normally unrealistic in practice.

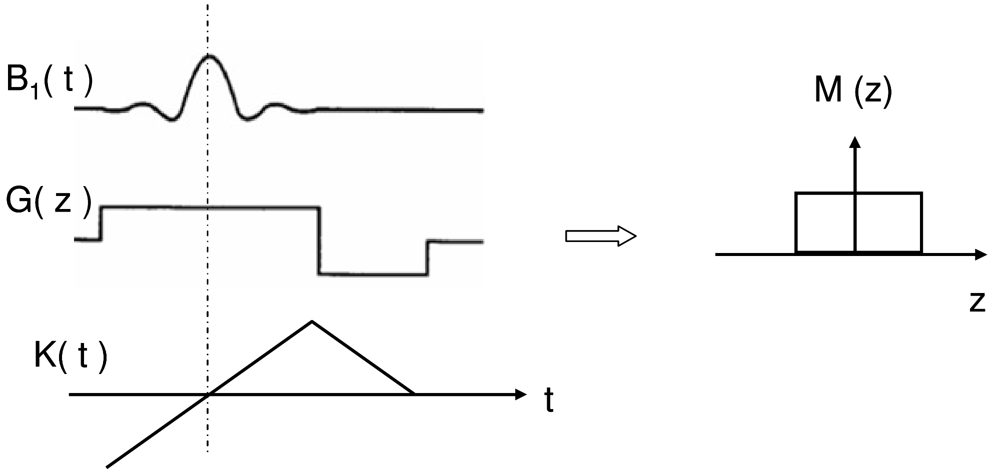

Figure 2.3. (Left) A small-tip angle ideal sinc RF pulse, gradient and corresponding k-space; (Right) Resulting rectangular slice profile (1).

In multidimensional spatially selective excitation, the gradient waveforms $\mathbf{G}(t)$ are not constant while the RF is applied. But the Fourier transform relationship between the B_1 weighting of k-space as determined by the gradient waveforms and the spatially excitation pattern, defined by Eq. (2.7), can still be valid. However, at higher dimensional spaces, the k-space cannot be covered completely, and a trajectory through k-space must be defined. The k-space trajectory must cover a sufficient region with an adequate density determined by Nyquist sample theorem. Figure 2.4 shows two commonly used k-space trajectories, EPI and spiral.

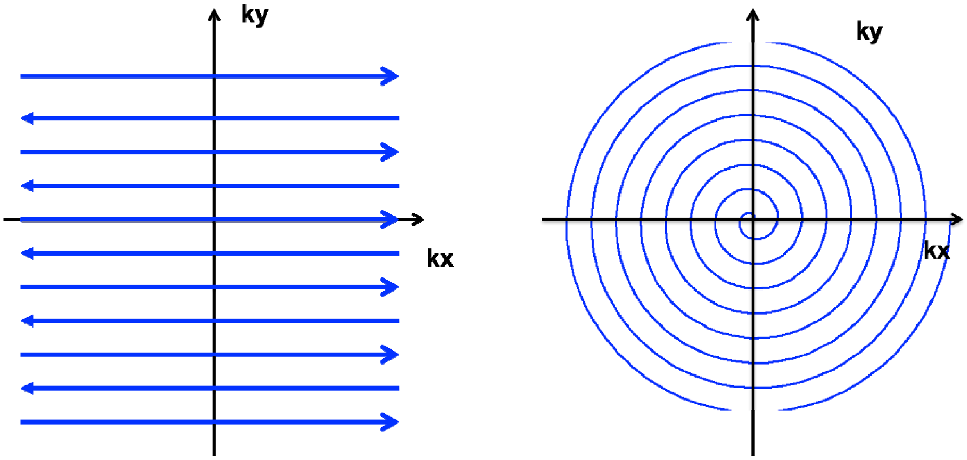

Figure 2.4. (Left) An EPI k-space trajectory and (Right) a spiral k-space trajectory.

Once a k-space trajectory is chosen, Eq. (2.7) can be rewritten by incorporating an integral over a 3D δ-function, which describes the k-space trajectory (1)

$$M_+\left(\mathbf{r},T\right)=i\gamma M_0\int_0^T dtB_1\left(t\right)\int d^3\mathbf{k}\,\delta^3\left(\mathbf{k}\left(t\right)-\mathbf{k}\right)e^{i2\pi\mathbf{k}\cdot\mathbf{r}} \tag{2.9}$$

and upon interchange of integration

$$\begin{aligned}M_+\left(\mathbf{r},T\right)&=i\gamma M_0\int d^3\mathbf{k}\left(\int_0^T dtB_1\left(t\right)\delta^3\left(\mathbf{k}\left(t\right)-\mathbf{k}\right)\right)e^{i2\pi\mathbf{k}\bullet\mathbf{r}}\\&=i\gamma M_0\int d^3\mathbf{k}B_1\left(\mathbf{k}\right)e^{i2\pi\mathbf{k}\bullet\mathbf{r}}\end{aligned} \tag{2.10}$$

The excitation pattern $M_+\left(\mathbf{r},T\right)$ is now the Fourier transform of the B_1 weighting of k-space and

$$B_1\left(\mathbf{k}\right)=\int dtB_1\left(t\right)\delta^3\left(\mathbf{k}\left(t\right)-\mathbf{k}\right) \tag{2.11}$$

In summary, to achieve the desired excitation pattern $M_+(\mathbf{r})$, the RF pulse $B_1(t)$, must be simultaneously applied along a k-space trajectory defined by the gradient waveforms. The excitation pattern will be the Fourier transform of the B_1 weighting of k-space.

To design a multidimensional spatially selective RF pulse, 2D excitation pulse for example, the steps are as follows:

1. Choose a k-space trajectory that approximately uniformly covers k-space as in Fig. 2.4. According to Nyquist sampling theorem, the maximum coverage of the k-space trajectory is determined by spatial resolution; and the sampling density of the k-space trajectory is determined by field of excitation in the spatial domain (FOX).

2. Find inverse Fourier transform of the excitation profile $M_+(\mathbf{r})$ along the chosen k-space trajectory.

3. The RF pulse is then designed according to Eq. (2.11).

3. INTRODUCTION TO PRINCIPLE OF PARALLEL EXCITATION

Multidimensional spatially selective excitation often involves the use of prolonged RF pulses to achieve desired spatial resolution and is limited by the performance of the gradient system. For example, clinical applications of 3D spatially selective excitation RF pulses typically require excitation RF duration to be about 20-30ms. Thus, its application is often hindered by the finite lifetime of the transverse magnetization caused by T2* relaxation effects.

To address this problem, parallel excitation techniques have been proposed to shorten such RF pulses duration by utilizing multi-channel transmit coils. As shown in Figure 3.1, given a parallel system that is composed of multiple transmit coils with independent RF pulse synthesizers and amplifiers, an orchestrated play of shorter RF pulses can achieve desired excitation profiles faster without adding strains to gradients by exploiting the localized sensitivities of the coils (5,7-8). Moreover, parallel excitation techniques offer the flexibility to further improve spatially selective excitation for applications like improving field inhomogeneity at high-fields.

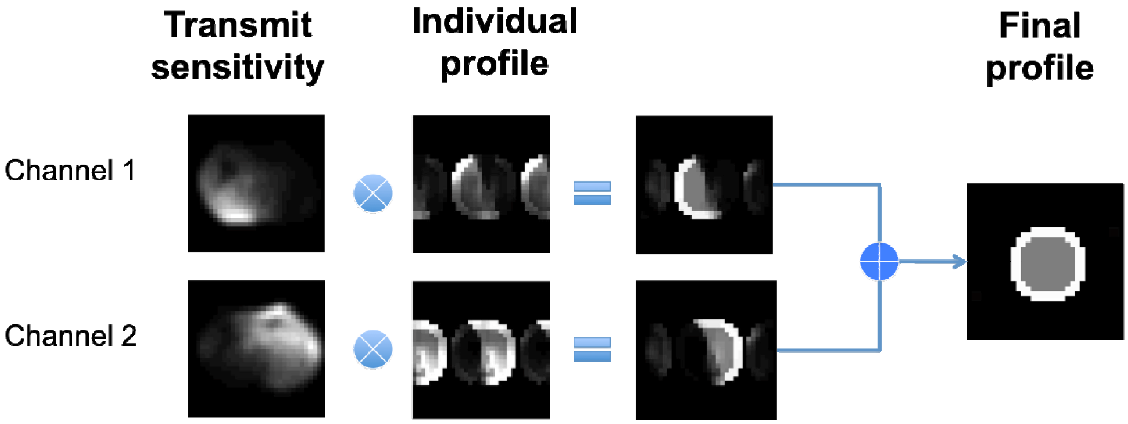

Figure 3.1. Illustration of the principle of parallel excitation.

Currently, there are three major parallel excitation design methods that are widely accepted, namely a method based on k-space domain proposed by Katscher termed “Transit SENSE”, a method based on both image and k-space domain weighting proposed by Zhu, and a method based on image domain only proposed by Grissom et.al. (5,7-8). In the following sections, these design methods will be described individually.

3.1 Transmit SENSE

“Transmit SENSE” in parallel excitation (7) was proposed in analogy to “SENSE” technique in parallel imaging (17). The underlying idea is that using multiple transmit coils, each of which exhibits a spatially different B_1 sensitivity pattern, the path to be traversed in excitation k-space, i.e., k-space trajectory can be undersampled. Each coil is driven by its own time-dependent RF waveform, thus the missing parts of the excitation k-space can be compensated and thereby shortening the RF pulses without sacrificing spatial resolution. Transmit SENSE RF pulses are designed in the k-space and the details are outlined in the following.

As introduced in Section 2, a desirable excitation pattern $M_{des}(\mathbf{r})$ can be excited by applying a complex RF waveform $B_1(t)$, accompanied by multidimensional gradient waveform $\mathbf{G}(t)$. The variable $\mathbf{r}$ denotes the multidimensional spatial coordinate, and t is the time coordinate. According to k-space analysis for small tip angle excitation in (1), the corresponding RF waveform can be calculated by Fourier transforming the desired pattern $M_{des}(\mathbf{r})$ into k-space $M_{des}(\mathbf{k}(t))$ (7)

$$B_1(t) = \frac{1}{M_0} \frac{|\mathbf{G}(t)|}{D(\mathbf{k}(t))} M_{des}(\mathbf{k}(t)) \tag{3.1}$$

where $D(\mathbf{k}(t))$ is the k-space sample density and $\mathbf{k}(t)$ is defined as the inverse time integral of the gradient waveform.

$$\mathbf{k}(t) = -\gamma \int_t^T \mathbf{G}(\tau)\, d\tau \tag{3.2}$$

Even though Eq. (3.1) was derived for small flip angle excitation, it could be valid even for large flip angle for certain k-space trajectories, e.g., the spiral one (1).

Let L be the number of transmit coils, each of which is with independent complex B_1 sensitivity profiles, $S_l(\mathbf{r})$, $l = 1,\ldots,L$. The desired excitation pattern $M_{des}(\mathbf{r})$ can be decomposed into the linear superposition of all the individual excitation patterns, weighted by the corresponding sensitivity profiles $S_l(\mathbf{r})$

$$M_{des}(\mathbf{r}) = \sum_{l=1}^{L} S_l(\mathbf{r}) M_l(\mathbf{r}) \tag{3.3}$$

where $M_l(\mathbf{r})$ is the individual excitation pattern generated by *l*-th transmit coil within the field-of-excitation (FOX). If the RF pulse duration is shortened by undersampling k-space trajectory, the resulting individual excitation patterns $M_l(\mathbf{r})$ will be aliased.

The central idea of Transmit SENSE is to utilize this linear superposition relationship in Eq. (3.3) to cancel out the aliasing artifacts associated with individual excitation patterns $M_l(\mathbf{r})$.

Equation (3.3) could be discretized in FOX as

$$M_{des}(\mathbf{r}_p) = \sum_{l=1}^{L} S_l(\mathbf{r}_p) M_l(\mathbf{r}_p) \tag{3.4}$$

with $\mathbf{r}_p$ denotes the spatial locations, $p = 1,\ldots,P$. After Fourier transform, Eq. (3.4) becomes

$$M_{des}(\mathbf{k}_p) = \sum_{l=1}^{L} S_l(\mathbf{k}_p) \otimes M_l(\mathbf{k}_p) \tag{3.5}$$

The convolution integral $S_l \otimes b_l$ can be expressed by a matrix/vector multiplication

$$M_{des}(\mathbf{k}_p) = \sum_{l=1}^{L} S_l(\mathbf{k}_p - \mathbf{k}_{p'}) M_l(\mathbf{k}_{p'}) \tag{3.6}$$

where $\mathbf{k}_{p'}$ denotes the k-space trajectory chosen. For a fully sampled k-space trajectory $\mathbf{k}_{p'}$ with length *P*, S_l are matrices of the size $P \times P$ and M_l is a vector of length *P*. The k-space trajectory $\mathbf{k}_{p'}$ can be chosen arbitrarily as long as they satisfy the sampling theorem and the given gradient and slew rate limit.

When the k-space trajectory $\mathbf{k}_{p'}$ is undersampled with acceleration (undersampling) factor *R*. The length of vector $M_l\left(\mathbf{k}_{p'}\right)$ becomes *P/R*. The size of matrix $S_l\left(\mathbf{k}_p - \mathbf{k}_{p'}\right)$ reduces to $P \times \left(P / R\right)$. Noted the acceleration factor *R* does not need to be equal to the number of coils used, *L*. For the ease of computation, Eq. (3.6) could be further combined into matrix/vector multiplication form

$$M_{des}\left(\mathbf{k}_p\right) = S_{full}\left(\mathbf{k}_p - \mathbf{k}_{p'}\right) M_{full}\left(\mathbf{k}_{p'}\right) \tag{3.7}$$

where $M_{full}\left(\mathbf{k}_p\right) = \left(M_1\left(\mathbf{k}_p\right), M_2\left(\mathbf{k}_p\right), \ldots, M_L\left(\mathbf{k}_p\right)\right)$

The combined vector M_{full} is unknown, and contains the k-space excitation profiles of all the channels. It can be solved from Eq. (3.7) by a straightforward matrix inversion. However, the sensitivity matrix S_{full} to be inverted could be ill-conditioned for undersampled k-space trajectories (18), thus it normally requires the help of regularization techniques, such as Tikhonov regularization (19) to solve Eq. (3.7).

$$M_{full} = S_{full}^{*}\left(S_{full} S_{full}^{*} + \lambda^2\right)^{-1} M_{des} \tag{3.8}$$

where λ represents the regularization parameter, and * denotes the transposed complex conjugate.

The conditioning of the matrix S_{full} is determined by the sensitivity profiles and the k-space trajectories chosen. As discussed by Katscher and colleagues in (18), the k-space sensitivity matrices S_{full} for Cartisian and spiral k-space trajectories, demonstrate different matrix conditioning. In the case of Cartisian k-space trajectory, S_{full} has a diagonal structure and regularization is not necessary. For spiral k-space trajectory, S_{full} is close to singular, requiring strong regularization. Regularization controls the frequency range in the solution, i.e., the larger λ, the smoother the solution M_{full} in the k-space. The optimum λ can be determined by, for instance, maximizing the correlation between the ideal input excitation pattern M_{des} and the numerical solution.

After calculating combined excitation profiles $M_{full}(\mathbf{k})$ in the k-space domain, individual excitation profile $M_l(\mathbf{k})$ can be extracted from $M_{full}(\mathbf{k})$. Then the time-domain RF pulse $B_{1,l}(t)$ could be derived using Eq. (3.1)

$$B_{1,l}(t_{p'}) = \frac{|\mathbf{G}(t)|}{M_0 D(\mathbf{k}(t))} M_l(\mathbf{k}_{p'}) \tag{3.9}$$

In Summary, the procedure of transmit SENSE is as follows:

1. Choose a desirable excitation profile $M_{des}(\mathbf{r})$ and a k-space trajectory $\mathbf{k}$
2. Measure the transmit sensitivity profiles for each individual channel $S_l(\mathbf{r})$ within the FOX.
3. Calculate the desirable excitation pattern and individual sensitivity profiles in the k-space, and construct the combined sensitivity matrix S_{full} and excitation profile M_{des}
4. Solve Eq. (3.7) and extract individual excitation profiles $M_l(\mathbf{k})$
5. Calculate individual RF pulse $B_{1,l}(t)$ using Eq. (3.9)

The feasibility of Transmit SENSE has been verified by both simulation and experiments (7,20). Other applications might benefit from the ability of Transmit SENSE to improve the spatial resolution of the pulse profile while maintaining the transmit duration. However, one constrain of Transmit SENSE is that for large flip-angle excitations, the possible choices of k-space trajectories are limited because of the constraint on Eq. (3.1). Moreover, the convolution of two k-space trajectories would be difficult to calculated for certain trajectories, such as spirals. Beyond Transmit SENSE, two other image-based parallel excitation techniques have been proposed and are more widely used as described in the next two sections.

3.2 Zhu's Method

Zhu proposed another RF pulse design technique for parallel excitation (5) simultaneously with Transmit SENSE, from the perspective of spatial and spatial-frequency domain weighting. The uniqueness of this method is that instead of assuming the transmit channels are perfectly decoupled; this method is capable of taking coil-coupling effect into consideration. Moreover, it's first RF design method that takes SAR management into consideration for parallel excitation.

Following the derivation of small-flip-angle excitation in Section 2, the transverse magnetization resulting from a single transmit coil may be analyzed by Fourier-transforming the k-space trajectory that is traversed and weighted during the excitation.

$$M(\mathbf{r}) = j\gamma M_0(\mathbf{r}) S(\mathbf{r}) \int_{\mathbf{k}} B_1(\mathbf{k}) P(\mathbf{k}) e^{j2\pi\mathbf{k}\cdot\mathbf{r}} \, d\mathbf{k} \tag{3.10}$$

where $P(\mathbf{k})$ represents the sampling scheme for a k-space trajectory constrained by gradient and slew rate limits, $B_1(\mathbf{k})$ is the RF energy weighting in the k-space, and $S(\mathbf{r})$ is the coil's transmit sensitivity pattern as in section 3.1.

Similar to transmit SENSE, when multiple independent transmit coils are used for driving RF sources, the excitation pattern is a result of linear superposition of individual excitation profiles from each channel weighted by the coil sensitivity patterns. However, in a more generous case, when the transmit coils are mutually coupled with each other, the superposition is also weighted by the mutual coupling coefficients, in addition to the coil sensitivity patterns. Thus, Eq. (3.10) can be extended to analyze the parallel excitation system based on the property of linearity

$$M(\mathbf{r}) = j\gamma M_0(\mathbf{r})\sum_{l=1}^{L} S_l(\mathbf{r}) \int_{\mathbf{k}} \sum_{m=1}^{L} c_{m,l} B_{1,m}(\mathbf{k}) P_m(\mathbf{k}) e^{j2\pi\mathbf{k}\cdot\mathbf{r}}\, d\mathbf{k} \tag{3.11}$$

where L denotes the total number of transmit coils, $c_{m,l}$'s are the mutual coupling coefficients between the l-th and m-th coils.

Following the derivation by Zhu in (5), the mutual coupling coefficients can be incorporated in the coil sensitivity profiles, and Equation (3.11) can be rearranged and rewritten to be

$$M(\mathbf{r}) = \sum_{m=1}^{L} \hat{S}_m(\mathbf{r}) \int_{\mathbf{k}} B_m(\mathbf{k}) P_m(\mathbf{k}) e^{j2\pi\mathbf{k}\cdot\mathbf{r}}\, d\mathbf{k} \tag{3.12}$$

where $\hat{S}_l(\mathbf{r}) = \sum_{m=1}^{L} c_{m,l} S_m(\mathbf{r})$, and denotes the effective B1+ field sensitivity profiles, which account for both the coil sensitivity and the coupling between coils.

Zhu's method also involves the choice of a k-space trajectory. However, this method is restricted to echo-planar trajectory only, because this allows the calculation of aliasing sidelobes in the undersampling k-space direction. Then Eq. (3.12) is solved as an optimization framework to suppress the aliasing sidelobes (5). For the purpose of RF power management, the optimization framework is formulated to minimize SAR, and subject to constrain imposed by Eq. (3.12).

Given the same excitation profile, the redundancy of the parallel system offers the capacity for possible excitation acceleration factors of up to *L*-fold. Zhu's parallel excitation method solves RF pulse jointly from image domain and k-space domain. It offers the capability to take inter-coil mutual coupling effect into consideration, and also provides a way to incorporate RF power deposition management in the framework while facilitating the faithful production of desired excitation profiles (5). The limitation for this method is that only echo-planar k-space trajectories could be used.

3.3 Grissom's Method

Grissom and colleagues proposed another parallel excitation method that is based on image domain (8). In contrast to the previous two methods, it allows more flexible selection of arbitrary k-space trajectory and direct design of RF pulse in time domain. In this dissertation, all simulations were carried out based on this method. The following is a brief review.

Let L be the number of transmit coils with known, complex transmit sensitivity profiles $S_l(\mathbf{r})$, $l = 1, 2, ..., L$. Similarly to previous two methods, according to linearity in the small tip-angle regime, the desired excitation pattern $M_{des}(\mathbf{r})$ would be the summation of individual excitation patterns from each coil, weighted by transmit sensitivities. Therefore,

$$M_{des}(\mathbf{r}) = i\gamma M_0(\mathbf{r}) \sum_{l=1}^{L} S_l(\mathbf{r}) \int_0^T B_{1,l}(t)\, e^{i\mathbf{r}\mathbf{k}(t)}\, dt \qquad (3.13)$$

where $B_{1,l}(t)$ denotes the RF waveform for the l-th channel. Discretizing the time and spatial coordinates, we have:

$$M_{des}(\mathbf{r}_p) = \sum_{l=1}^{L} S_l(\mathbf{r}_p) \sum_{q=1}^{Q} i\gamma M_0(\mathbf{r}_p) B_{1,l}(q\Delta t) e^{i\mathbf{r}_p \mathbf{k}(q\Delta t)} \Delta t \qquad (3.14)$$

where $\mathbf{r}_p$ is the spatial grid, $p = 1, 2, ...P$ is the index of the P spatial grid points, Δt is the time sampling interval, and $q = 1, 2, ..., Q$ is the index of the Q time samples. The value of Δt should be determined by the time step used by the pulse sequence in the scanner. The spatial grid definition is mainly limited by the affordable computer memory and computation power. Equation (3.14) can be rewritten in a matrix form

$$[M_{tot}] = \sum_{l=1}^{L} [S_l] \bullet ([A][B_l]) \qquad (3.15)$$

where $[M_{tot}]$ is a $P\times 1$ vector containing all discretized spatial points, $[S_l]$ is a $P\times 1$ vector, and $\bullet$ stands for element-by-element multiplication. The matrix $[A]$ has a dimension of $P\times Q$ where its element is given by $a_{pq} = i\gamma M_0(\mathbf{r}_p) e^{i\mathbf{r}_p \mathbf{k}(q\Delta t)} \Delta t$ and $[B_l]$ is a $Q\times 1$ vector corresponding to the discrete-time samples of RF pulse of the l-th channel. Equation (3.15) can be further written as

$$[M_{tot}] = [C_1 \mid C_2 \mid ... C_L] \begin{bmatrix} B_1 \\ B_2 \\ \vdots \\ B_L \end{bmatrix} = C_{full} B_{full} \qquad (3.16)$$

where C_l is a $P \times Q$ matrix with $c_{pq} = i\gamma M_0(\mathbf{r}_p)\Delta t S_l(\mathbf{r}_p) e^{i\mathbf{r}_p\mathbf{k}(q\Delta t)}$, and B_{full} is the $(Q \times L) \times 1$ vector containing concatenated RF waveforms of all channels.

With this formulation, given a desired excitation pattern M_{des} and a k-space trajectory, the desirable RF pulses for parallel excitation can be calculated by

$$\hat{B}_{full} = \arg\min_{B_{full}} \left\{ \left\| C_{full} B_{full} - M_{des} \right\|_W^2 + B_{full}^* \Lambda B_{full} \right\} \tag{3.17}$$

where the diagonal matrix W can be used to define region of interest (ROI), i.e., put weights on spatial pattern, $B_{full}^* B_{full}$ is actually the accumulated RF power, $\Lambda = diag(\lambda_q^2)$, with λ_q as regularization parameter which can be used to control the RF power. The regularization parameter controls the compromise between RF power and excitation error.

In the following Sections 4 and 5, we will adopt Grissom's method as basis for parallel excitation RF pulse design. Eq. (3.17) will be solved using the conjugate gradient method, and the value of λ_q is chosen according to the maximal singular value of C_{full} matrix (i.e., $0.01\lambda_{\max}$)

3.4 SAR Problems Associated with Parallel Excitation

While parallel excitation using multiple transmit coils allows accelerating the time required for spatially selective RF pulses, one accompany problem would be elevated RF power deposition that could have a significant impact on the design of excitation pulses.

Increased RF power and corresponding high specific absorption rate (SAR) has become a severe problem limiting the clinical application of parallel excitation at high-field MRI.

As described in Section 2, in order to achieve a desirable excitation pattern and flip angle, certain RF pulses and gradient waveforms need to be supplied by the RF amplifier and transmitter. Energy deposited by RF pulses causes biological tissue heating (21-22). The International Electrotechnical Commission (IEC) standard and Food and Drug Administration (FDA) have adopted the specific absorption rate (SAR) as the metric for RF power safety for performing MRI procedures. The SAR is defined as the RF power absorbed per unit mass of an object and is measured in watts per kilogram (W/kg). For example, the SAR limit in the FDA guideline is 4 W/kg averaged over the whole body for any 15-min period, 8 W/kg in any gram of tissue in the extremities for any period of 5 min, and 3 W/kg averaged over the head for any 10-min period, provided the maximal instantaneous SAR does not exceed 4 W/kg (23-24).

$$SAR(\mathbf{r})=\frac{\sigma(\mathbf{r})}{2\rho(\mathbf{r})}\left\|\mathbf{E}(\mathbf{r})\right\|^{2}$$

where $\sigma(\mathbf{r})$ and $\rho(\mathbf{r})$ is tissue dielectric property and tissue density at spatial location $\mathbf{r}$, $\mathbf{E}(\mathbf{r})$ is the corresponding electric field scaled by RF pulse.

Since parallel-excitation techniques are of great interest at high fields, it is specifically notable that first-order SAR increases quadratically with B0 field strength (25). Thus, the energy deposited by a 90° pulse in the sample can be fourfold higher at 3 T than at 1.5 T. In addition, Katscher et al. (20) showed that the RF power needed for parallel excitation pulses for certain array geometries increased quadratically with the pulse duration reduction factor for a fixed flip angle when the ratio N/R (where N is the number of coils, and R is the reduction factor) is large. With small N/R ratios, the behavior of SAR is more complex, but still increases significantly with R. And this elevation of SAR with regard to reduction factor R has been verified in many simulation studies (9,20,26).

Moreover, for parallel excitation with multi-channel transmit coils, the SAR becomes

$$\begin{aligned} SAR(\mathbf{r}) &= \frac{\sigma(\mathbf{r})}{2\rho(\mathbf{r})}\frac{1}{T}\int_0^T \left\|\mathbf{E}_{tot}(\mathbf{r},t)\right\|^2 dt \\ &= \frac{\sigma(\mathbf{r})}{2\rho(\mathbf{r})}\frac{1}{T}\int_0^T \left\|\sum_{l=1}^{L}\mathbf{E}_{l0}(\mathbf{r})B_{1,l}(t)\right\|^2 dt \end{aligned} \tag{3.18}$$

where $\mathbf{E}_{l0}(\mathbf{r})$ is the spatial distribution of the electrical field of a single coil at a given load for a current of unit amplitude. $B_{1,l}(t)$ is the individual RF waveform for the *l*-th coil. At high-fields, the magnetic and electric field distributions become more complex because of the shortened wavelength and the dielectric properties of the tissues (27-28). The complex effect of electric field generated from all transmit channels in parallel excitation could interact and superimpose with each other and create localized ”hot spots” that are difficult to control (29).

For these reasons, SAR is a critical problem that needs to be addressed to facilitate the transition of parallel excitation techniques from research laboratories to high-impact clinical applications. In the next two sections, we will be focusing on introducing two methods to design RF pulse and corresponding k-space trajectories to reduce SAR in parallel excitation.

4. VARIABLE-DENSITY TRAJECTORY DESIGN FOR PARALLEL EXCITATION

In parallel excitation, the localized transmit coil sensitivities can be utilized for sparse sampling of the excitation k-space, thereby reducing the pulse duration. The simultaneously transmitted RF waveforms from multi-channel transmit coils need to be proper designed for two purposes: 1) to eliminate the aliasing caused by undersampling of the excitation k-space for image quality control; and 2) to reduce the elevated RF power, or SAR within regulation limit for patient safety control.

Several methods using regularization in RF pulse design have been proposed to balance SAR and the accuracy of the excitation pattern by minimizing a cost function that incorporates both excitation error and the RF power (5,8,26,30).

One of the flexibilities in parallel excitation that has not been fully explored for SAR reduction, however, is the selection of excitation **k** space trajectory. The spatial distribution and the SAR can be influenced by both the desirable excitation pattern and the selected k-space trajectory (31). Currently, constant-density (CD) spirals and echo-planar imaging (EPI) seem to be the k-space trajectories of choice for parallel excitation in the literatures (5,7-8), and a method has been reported for jointly optimizing the RF pulse and k-space trajectory (32-33). The method parameterizes an EPI trajectory along one dimension and alternates between optimizing the pulses and adjusting the trajectory parameters. Our group has previously reported preliminary results using variable-density (VD) spirals for parallel excitation (34). VD spirals, a k–space trajectory initially proposed for imaging, can also be used in parallel excitation to provide improved combined performance with respect to SAR and excitation pattern. For single-channel imaging, the advantages of VD spiral sampling have been demonstrated in various applications such as increased temporal resolution of MR fluoroscopy, reduced motion artifacts in cine imaging, reduced side-lobes in impulse response and reduced total energy of spatial aliasing artifacts (35-37). It has also been shown that VD spirals can be applied to shorten three-dimensional (3D) tailored RF pulses with small tolerable errors in selective excitation (38). Most of the previous work has been applied to single-channel excitations, however. Variable-rate selective excitation (VERSE), a method previously proposed for RF power reduction in one-dimensional slice-selective RF pulses (1), has been extended to 2D selective excitation (39) and to Transmit SENSE (33). The basic idea of the method is to adaptively adjust the gradient to reduce the slew rate in the central k-space region.

In this section, we adopt a related but more flexible approach for SAR reduction in parallel-excitation pulse design (i.e., using spiral k-space trajectories with both variable radial and adjustable angular rates). Parallel excitations with CD and VD spirals were studied using numerical simulations (34). The parallel RF pulses were designed using a direct discretization spatial-domain method proposed by Grissom et al (8). Resulting excitation patterns were generated using a Bloch simulator developed by Pauly at

Stanford University (http://www.stanford.edu/class/ee469b/mfiles/), and SAR distributions were evaluated quantitatively. The SAR and excitation pattern quality were studied for different reduction factors and for different excitation profiles. The results show that, for the same pulse duration and $\mathbf{k}$ -space coverage, parallel excitation with VD spirals results in a much more reduced SAR compared with CD spirals. The lowered SAR comes with slight but noticeable degradation of the spatial resolution of the excitation pattern, but the artifact power in the excited pattern is reduced.

4.1 Spiral Design

One important degree-of-freedom in parallel excitation pulse design is the choice of k-space trajectory. Due to high time efficiency and reduced strain on the gradient system, spiral trajectories are widely-used in parallel excitation. In this work, we develop a method for parallel excitation using VD spirals and show that it is possible to achieve significantly reduced SAR using this approach. A number of VD spiral trajectories have been proposed in the literature (32,34,36-37). In our study, we chose the empirical approximation method described in (37) because it has a parametric control of the density and incorporates the gradient constraints in the trajectory design. Specifically, the k-space trajectory is defined as

$$k\left(t\right)=k_{\max}\tau\left(t\right)^{\alpha}\exp\left(i2\pi N\tau\left(t\right)\right) \tag{4.1}$$

where $k_{\max}$ is the maximal k-space radius covered [determined by $k_{\max}=1/\left(2\Delta r\right)$ where Δr is the excitation resolution], τ(t) is the normalized temporal parameterization of the trajectory, α is the parameter controlling VD spiral and N is the number of spiral revolutions that will be determined by (Eq. 3.6). For spatially selective excitation, spiral-in trajectories are more desirable, in which case τ(t) decreases monotonically, and τ(0)=1 and τ(T)=0, where T is the pulse duration. The gradient constraints are incorporated by adjusting τ(t) according to maximal gradient and slew rates. The spirals are designed following the method described in Kim et al. (37). Specifically, for a spiral-out trajectory

$$\hat{\tau}(t)=\begin{cases}\left[\sqrt{\dfrac{s_m\gamma}{k_{\max}(2\pi N)^2}}\left(\dfrac{\alpha}{2}+1\right)t\right]^{\left[\frac{1}{(\alpha/2+1)}\right]} & 0\le t\le \min\left(T_{s2a},T_{es}\right)\\ \left[\dfrac{\gamma G_m}{k_{\max}(2\pi N)}(\alpha+1)t\right]^{1/(\alpha+1)} & T_{s2a}\le t\le T_{ea}\end{cases} \tag{4.2}$$

where s_m is the maximal gradient slew rate, G_m is the maximal gradient amplitude, $k_{\max}$ is the maximal k-space radius covered and γ is the gyromagnetic ratio. In the above equation, T_{ea} is the ending time for the trajectory subjected to amplitude constraint only.

$$T_{ea}=\left[\frac{\gamma G_m}{k_{\max}(2\pi N)}(\alpha+1)\right]^{-1} \tag{4.3}$$

T_{es} is the ending time of the trajectory subjected to the slew rate constraint only

$$T_{es}=\left[\left(\frac{\alpha}{2}+1\right)\sqrt{\frac{s_m\gamma}{k_{\max}(2\pi N)^2}}\right]^{-1} \tag{4.4}$$

Finally, T_{s2a} is the time that the trajectory switches from the slew-rate-limited regime to the amplitude-limited regime

$$T_{s2a} = \left[\frac{G_m \gamma}{\lambda\omega \frac{1}{\alpha/2+1}\left(\left(\frac{\alpha}{2}+1\right)\sqrt{\frac{s_m \gamma}{\lambda\omega^2}}\right)^{[(\alpha+1)/(\alpha/2+1)]}} \right]^{\frac{(\alpha+2)}{\alpha}} \tag{4.5}$$

In our simulation, spiral-in trajectories are used. Therefore, $\tau(t) = \hat{\tau}(T-t)$, where $T = \min(T_{es}, T_{ea})$ is the pulse duration.

In fact, methods were developed using the VERSE principle modify τ(t) to traverse at a slow slew rate in the central k-space (33,39). This principle is also used in this study. However, in addition to this adjustment, the parameter α is used to control the radial density of the spirals (e.g., α=1: CD spiral; α=2: VD spiral with central k-space that is twice as dense as the outer k-space). A maximal gradient G_m and a slew rate s_m can be specified less than the system limit according to the VERSE principle. To our knowledge, there is no analytical method for optimal parameter selection of α. Therefore, a range of α values from 1 to 4 are tested. For fully sampled spiral k-space trajectory, N is determined by field of excitation (FOX) and desired spatial resolution Δr [i.e., by solving k(1)−k((N−1)/N)=1/FOX for Nyquist sampling]

$$N = \frac{1}{1-\left(1-\frac{2\Delta r}{FOX}\right)^{1/\alpha}} \tag{4.6}$$

where FOX is defined as the distance from the field-of-view (FOV) center to the first side lobe.

For parallel excitations, the spiral trajectory is undersampled, i.e., with fewer turns than non-accelerated k-space trajectory. In this dissertation, the undersampling factor (also called acceleration factor) R is defined as the ratio of pulse durations, with and without k-space undersampling. For CD spirals with constant slew rate, R corresponds to the reduction of the number of spiral revolutions due to undersampling. As an illustration, Figure 4.1 shows a CD spiral, a VD spiral, and the corresponding undersampled spirals with a factor of $R = 2$.

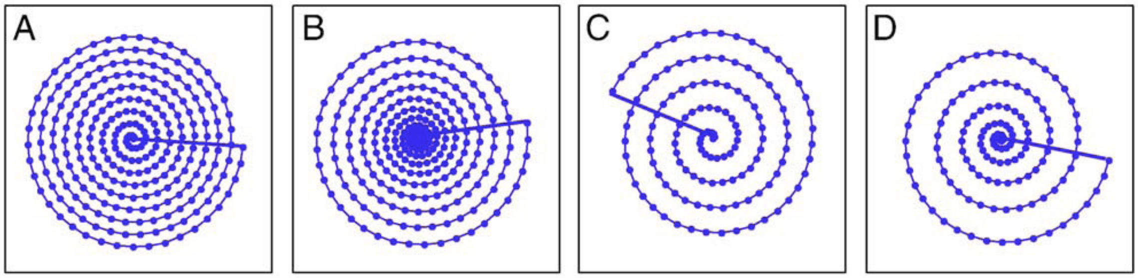

Figure 4.1. Illustration of the spiral trajectories. (A) A CD spiral (α=1, R=1). (B) A VD spiral (α=2, R=1). (C) The undersampled CD spiral (α=1, R=2). (D) The undersampled VD spiral (α=2, R=2).

For typical excitation patterns, the k-space energy spectrum is concentrated in low-frequency region of k-space. Therefore, a VD spiral that allocates more time to the central region of k-space will reduce the magnitude of an RF pulse required to achieve a certain tip angle and correspondingly, reduce the magnitude of the electric field by the same amount. Thus, VD spirals can potentially lead to reduced SAR (proportional to $|E|^2$).

4.2 Transmit Electromagnetic Field Simulation

Simulated electromagnetic field was used for the pulse design and SAR evaluation in the parallel excitation. In particular, a four-channel transmit coil and a 3D head model with known dielectric properties and tissue density were modeled at 4.7 Tesla (200 MHz) using a FDTD software, xFDTD 6.3 bio-pro package (Remcom Inc. State College, PA). The coil configuration and relative position to the head are illustrated in Fig. 4.2. Each element (rung) is driven by an ideal current source at one end and tuned to series resonance by a capacitor on the other end. The modeled dimensions of the coil are: radius of rung = 140 mm, length of rung = 250 mm, and width of rung = 20 mm. The radius of the shield is 165 mm. The 3D head model is located in the center of the RF shield. Ideal RF current sources at 200MHz are fed at one end of each rung in the simulation for inter-coil decoupling (40). For the field simulations, a human head mesh included in the xFDTD software package was used.

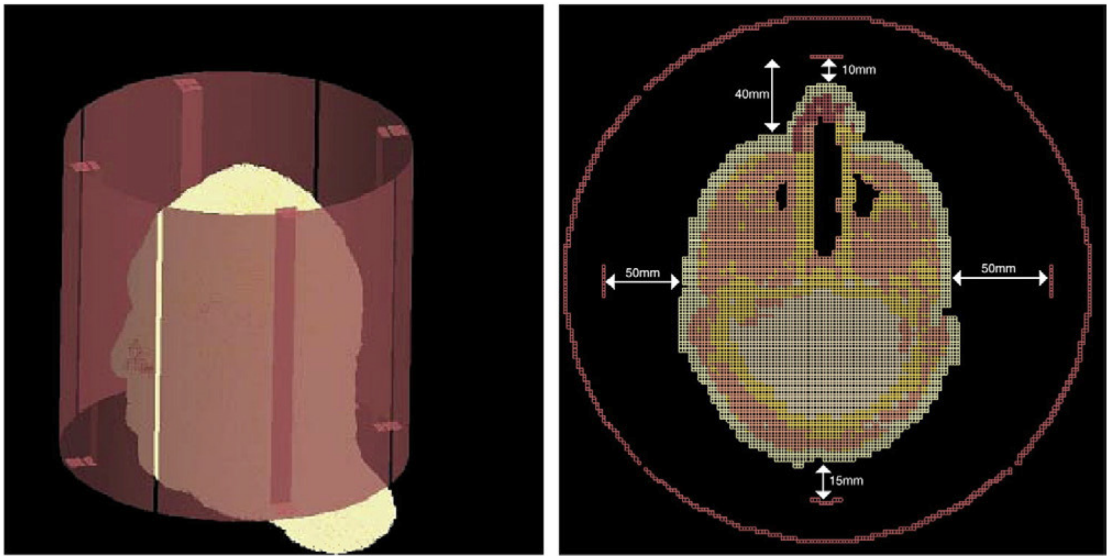

Figure 4.2. Top view showing the relative locations of the head model, RF shield and coil elements. The rung (bars) in the side view represents the coil elements. The 3D head model is located at the center of the RF shield. The radius of the shield is 165 mm.

The xFDTD output gives the steady state 3D B field and E field sensitivity produced by a constant excitation (Fig. 4.3). These are then scaled according to the RF pulse excitation waveform to determine the time dependent fields. The magnitude of the transmit E and B fields of the four-channel coil at a mid-axial slice in the head model are shown in Fig. 4.3. The actual channel coupling is less than -20 dB. The effective component of the magnetic field ($B_x + jB_y$ or $B_x - jB_y$, depending on the polarization used) was used as the transmit sensitivity $S(\mathbf{r})$ in the RF pulse design [see Eq. (3.7)]. After the RF waveforms were calculated, the total B field at any spatial point was determined as the sum of the RF waveforms weighted by B field sensitivity $S(\mathbf{r})$. Similarly, the total E field was determined by the sum of the RF waveforms weighted by the 3D E field sensitivity.

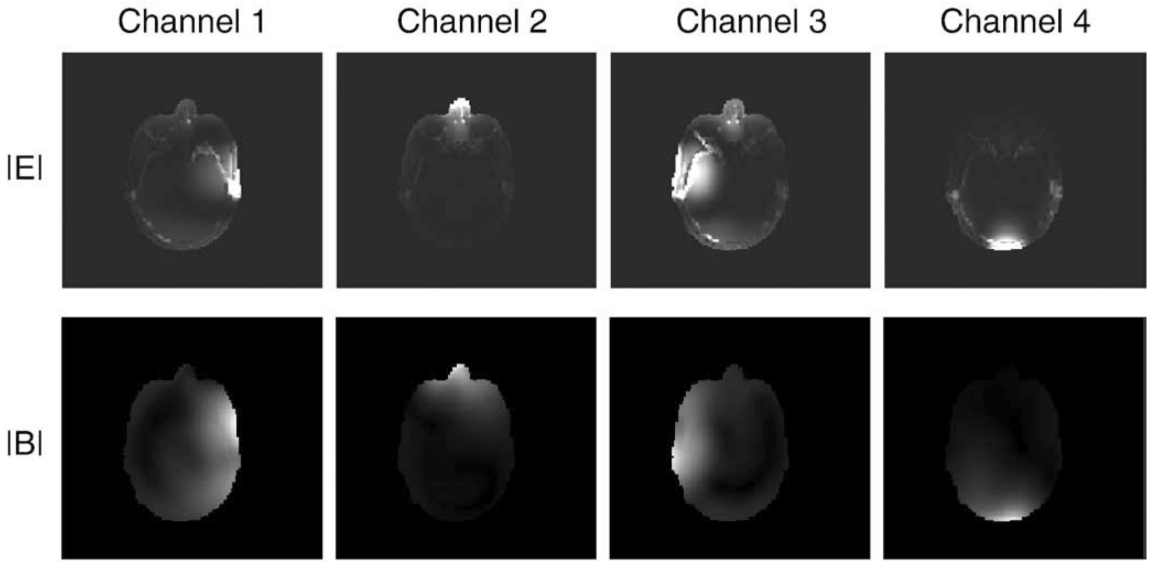

Figure 4.3. The E and B fields of a mid-axial slice in the simulated four-channel head transmit system. Top: E-field distribution. Bottom: B-field distribution. Only the magnitudes of the two transverse components are shown. Both E and B fields were masked with a binary head-shaped mask and windowed for better visualization. Some coupling effect can be seen after scaling up the fields, but the actual channel coupling is less than –20 dB.

4.3 Parallel Excitation Design and Simulations

Based on the small-tip-angle excitation approximation, the transverse magnetization generated by a selective excitation pulse at time T can be expressed as

$$M(\mathbf{r}) = i\gamma M_0(\mathbf{r}) \sum_{l=1}^{L} S_l(\mathbf{r}) \int_0^T B_{1,l}(t) e^{\mathbf{irk}(t)}\, dt \tag{4.7}$$

where γ denotes the gyromagnetic ratio, $M_0(\mathbf{r})$ is the equilibrium magnetization at the spatial coordinate **r**, $S_l(\mathbf{r})$ is the *l*th channel's complex transmit sensitivity, $B_{1,l}(t)$ is the complex RF pulse waveform (i.e., envelope) and $\mathbf{k}(t)$ is the excitation k-space trajectory (defined as the time-reversed integration of the gradient waveform played simultaneously with the RF pulse as in Pauly et al. (1)). As shown in Grissom et al. (8), given a desired excitation pattern M_{des} and a k-space trajectory, the desirable RF pulses for parallel excitation can be calculated by discretizing and solving Eq. (4.7)

$$\hat{\mathbf{B}}_{full} = \arg\min_{\mathbf{B}_{full}} \left\{ \left\| C_{full}\mathbf{B}_{full} - M_{des} \right\|^2 + \mathbf{B}_{full}^{*}\Lambda\mathbf{B}_{full} \right\} \tag{4.8}$$

where $C_{full} = [C_1 \mid C_2, ..., C_L]$, with C_l being a P×Q matrix with element $c_{pq} = i\gamma M_0(\mathbf{r}_p)\Delta t S_l(\mathbf{r}_p) e^{i\mathbf{r_p}\mathbf{k}(q\Delta t)}$, where $\mathbf{r}_p\,(p = 1, 2, ...P)$ is the spatial grid with the index of the *P* spatial grid points, Δt is the sampling time interval and *q* = 1,2,…,*Q* is the time index. The spatial grid definition is somewhat arbitrary, but is mainly limited by the affordable computer memory and computation power.

In the above equation, $\mathbf{B}_{full}$ is a $(Q \times L) \times 1$ vector containing concatenated RF waveforms of all L channels. The regularization parameter Λ can be used to control the compromise between RF power and excitation error. In this study, since we are studying the RF power behavior with different excitation k-space trajectories, we chose $\Lambda=0$ to eliminate the effect of the regularization on RF power. The solution to Eq. (4.8) can be obtained rather efficiently using the conjugate gradient method as described in Sutton et al. (41).

For our studies, a maximum gradient of 2.2 Gauss/cm and a maximum slew rate of 18 Gauss/cm/ms were used to constrain the gradient waveform and spiral trajectory. The number of revolutions N was determined according to Eq. (4.6) with $\Delta\mathbf{r}$ = 5 cm and FOX = 18 cm for all the excitation profiles. For the accelerated cases, the pulse durations are reduced by a factor of R. To design the RF pulses for the four parallel channels, the entire FOV was discretized to a 64×64 rectilinear grid. The RF pulse was sampled with a sampling interval of Δt = 5 μs. The RF waveforms were calculated using Eq. (4.8). Subsequently, the total B field was produced by the sum of RF waveforms weighted by field sensitivity $S(\mathbf{r})$, which was then input to a Bloch simulator to generate the excitation profile. The image acquisition FOV used in the Bloch simulator was 32×32 cm^2. To improve visualization, the Bloch simulation was performed with a resolution of 0.25 cm, half of the excitation resolution.

To compare VD spiral with CD spiral, we performed a sequence of simulations. For fair comparison, the constant-density spirals and variable-density spirals in this study covered the same k-space area, had the same pulse durations, and were scaled so that they achieve the same overall tip-angle.

Three excitation patterns were chosen for testing purposes: two squares of different sizes and a pattern with a complex phase map [see Fig. 4.4 (a-c)]. The first two tested the performance of the VD spirals under relatively wide and narrow k-space energy concentrations. The third tested the performance of an RF pulse that might be used for improving B0 field homogeneity.

Simulation I: 9×9 cm^2 Square Excitation Pattern

This simulation was used to compare the SAR of CD and VD RF pulses for a relatively large excitation pattern. The excitation pattern was designed to be a square (9×9 cm^2) with flip angle 5° in the center of the FOV as shown in Fig. 4.4(a). A CD spiral and a VD spiral with $\alpha=2$ were used. Both trajectories cover the same k-space area ($k_{\max}=1/\left(2\Delta\mathbf{r}\right)$, where $\Delta\mathbf{r}$ = 1 cm). The number of revolutions, N in both spirals were determined by Eq. (4.2) with FOX = 18 cm. However, for the VD spirals, the number of revolutions N was adjusted so that its pulse duration was the same as that of the CD spiral. Then the simulation was carried out for acceleration factors R = 1, 2, 3 and 4, and for both CD spiral (α = 1) and VD spirals (α = 2, 3 and 4).

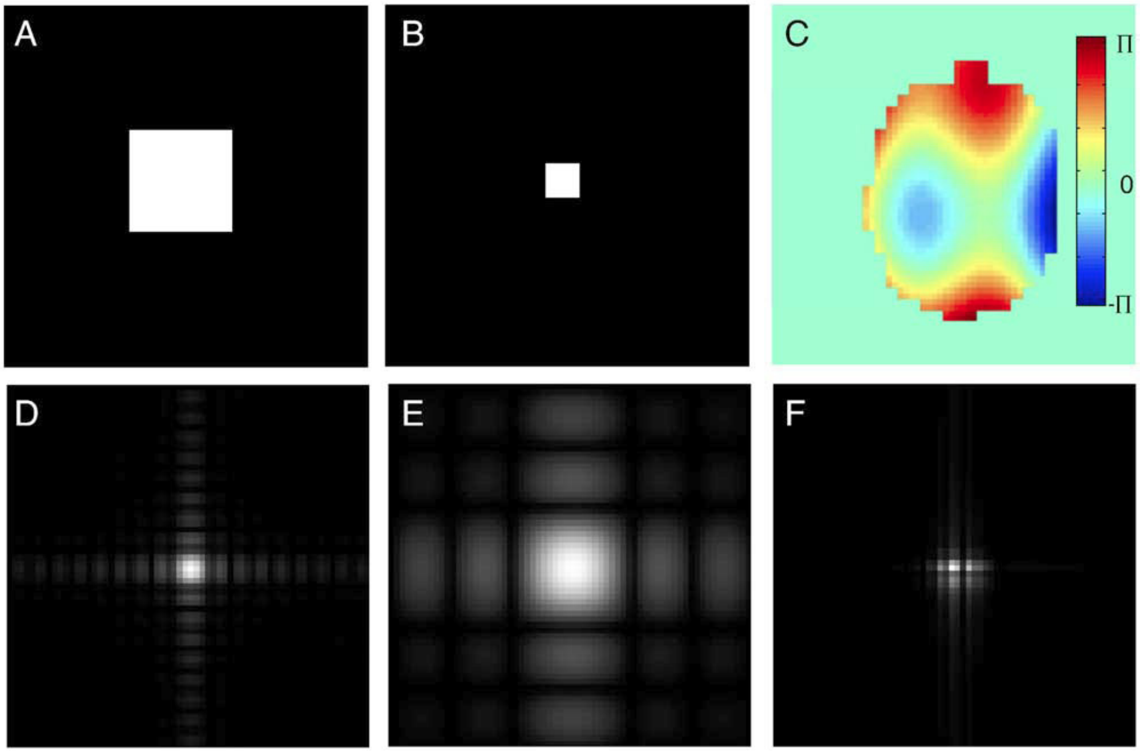

Figure 4.4. Three excitation patterns used in simulations. (A) a large square (9x9 cm^2) with zero phase (Simulation I); (B) a smaller square (3x3 cm^2) with zero phase (Simulation II); (C) a phase map (in radians) of the head with constant magnitude (Simulation III); (D–F) the corresponding **k**-space energy spectrum (magnitude) of the three excitation patterns shown in (A)–(C), respectively.

Simulation II: 3×3 cm^2 Square Excitation Pattern

The purpose of this simulation was to show the effects of VD spirals for a relatively small excitation pattern. In this study, the excitation pattern was designed to be a single block (3×3 cm^2) in the center of the FOV with flip angle 5° as shown in Fig.

4.4(b). As in simulation I, all trajectories covered the same k-space area ($k_{\max} = 1/(2\Delta r)$, where $\Delta\mathbf{r}$ = 1 cm), and the simulation was carried out for acceleration factors of R = 1, 2, 3 and 4 for both CD and VD spirals.

Simulation III: 32×32 cm^2 phase pattern

In this study, the CD spiral and the VD spiral were compared for exciting a complex phase pattern with a constant flip angle of 5°. This example tests the performance of VD pulses in a case that might arise when using parallel excitation for B0 field inhomogeneity compensation (8,42). A field map was incorporated to counteract the phase dispersion due to B0 field inhomogeneity. The desirable phase map was simulated as a slowly varying sinusoidal function in both x and y directions, as shown in Fig. 4.4(c). Simulations were carried out with the same parameters as in Simulations I and II.

4.4 SAR and Excitation Evaluation

RF power deposition in biological tissues depends on both the total electric field and the tissue properties. Specifically, at each spatial point, it is possible to evaluate the SAR as the time-averaged value over the pulse duration using the formula provided in Zhu (5) and Katscher et al. (10):

$$SAR(\mathbf{r}) = \frac{\sigma(\mathbf{r})}{2\rho(\mathbf{r})} \frac{1}{Q} \sum_{q=1}^{Q} \left\| \sum_{l=1}^{L} \mathbf{E}_l(\mathbf{r}) B_{1,l}(q\Delta t) \right\|^2 \tag{4.9}$$

where σ denotes tissue conductivity, ρ is tissue density, Q is the total number of time points, $\mathbf{E}_l(\mathbf{r})$ is the electric field sensitivity of the lth channel and $B_{1,l}$ is the corresponding RF waveform. In all simulations, the RF pulses were scaled so that the average tip angle over the excitation pattern was 5°(small-tip angle). After the SAR had been generated for all 3D grid points, an average SAR (i.e., spatially and temporally averaged SAR) was computed by averaging the time-averaged SAR maps over the whole 3D brain volume.

To qualitatively verify the RF pulse design and SAR evaluation procedures used in our studies, we first performed a simulation similar to the one described by Katscher et al. (20) using the same setup and parameters. Both coils were assumed to be perfectly decoupled, and each coil was modeled as a circular loop with a diameter of 20 cm. An FOV of 20 cm was used, and the distance between the coil and the FOV was 5 cm. The electric and magnetic fields were simulated using xFDTD with a main magnetic field of 3 T and then discretized into a 32×32 grid.

To quantitatively evaluate the excitation effects, excitation artifact power (AP) was computed to measure the difference between the desired pattern and the excitation pattern obtained from the Bloch simulator. Specifically, AP is defined as

$$AP = \frac{\sum_{\mathbf{r}} W(\mathbf{r}) \left| \hat{M}(\mathbf{r}) - M(\mathbf{r}) \right|^2}{\sum_{\mathbf{r}} W(\mathbf{r}) \left| M(\mathbf{r}) \right|^2} \tag{4.10}$$

where W(**r**) is a binary mask that is 1 inside the head and 0 in the background area, $\hat{M}(\mathbf{r})$ is the excited pattern and $M(\mathbf{r})$ is the desired pattern. For Simulation III, the primary concern is the phase of the excitation pattern. To evaluate the phase of the excited pattern, phase error (pErr) was defined as

$$pErr = \sum_{\mathbf{r}} W(\mathbf{r})\left(\arg\left(\hat{M}(\mathbf{r}) \cdot M^{*}(\mathbf{r})\right)\right) \tag{4.11}$$

where arg(·) is the phase function that returns the principal phase of its argument in the range of [−π, π), and $*$ denotes the complex conjugate operation.

4.5 Results

SAR verification

For qualitative comparison, Figure 4.5 shows two SAR distribution maps, with the two transmit coils placed at angles of 180° and 90°, respectively. The top two images are directly adapted from the original article (20) (with permission from Springer), and the bottom images are from our simulation. Good agreement can be seen between the two. Following this methodology verification, the three experiments previously described (Simulations I, II and III) were carried out using the method developed for parallel excitation with CD and VD spirals. The results for the three simulations are summarized below.

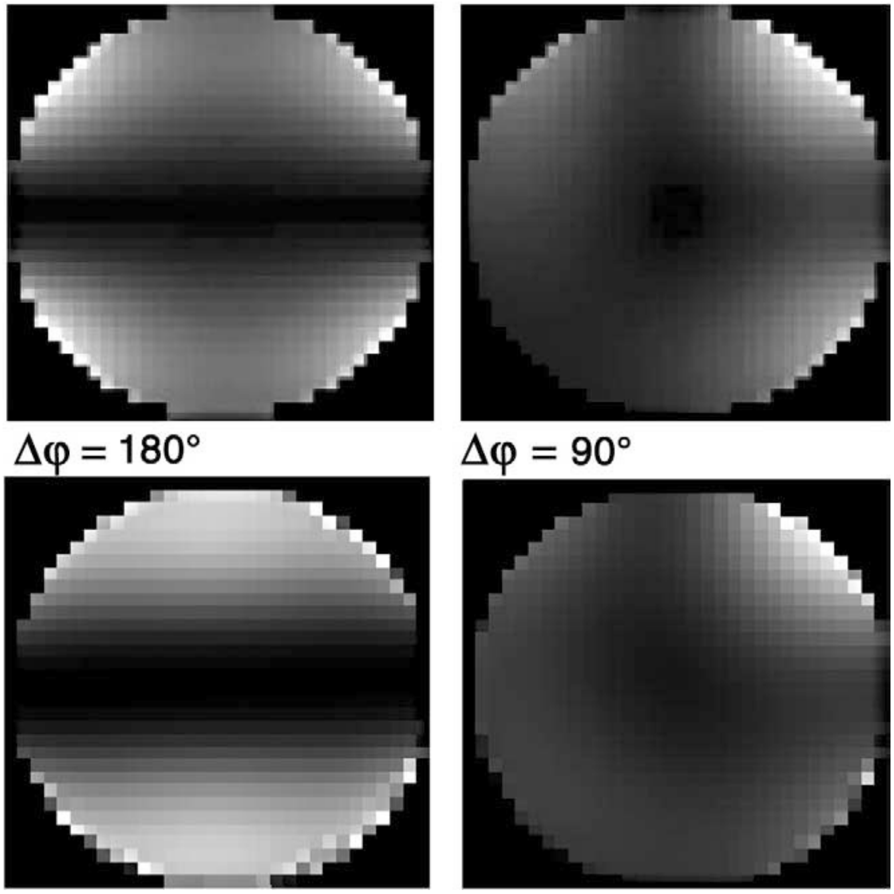

Figure 4.5. The SAR maps in a simulated study adapted from (upper) the results reported by Katscher et al. (20) (with permission from Springer) and (bottom) the corresponding results by our simulation. The left and right columns correspond to configurations, with the two transmit coils placed at angles of 180° and 90°, respectively. This study was used to qualitatively verify the simulation method used in this article.

Simulation I

Figure 4.6 shows the excitation patterns with a reduction factor R from 1 to 4 using CD ($\alpha = 1$) and VD ($\alpha = 2$) spirals. With the same k-space coverage and the same pulse duration, the excitation patterns show reduced AP by using VD spirals rather than CD spirals, especially for high acceleration factors (*R*=3 and 4). Specifically, the artifacts outside the selected excitation region were reduced. This improvement comes with a slight but noticeable loss in resolution, however. This is due to the fact that the outer k-space region is covered with reduced density when using VD spirals.

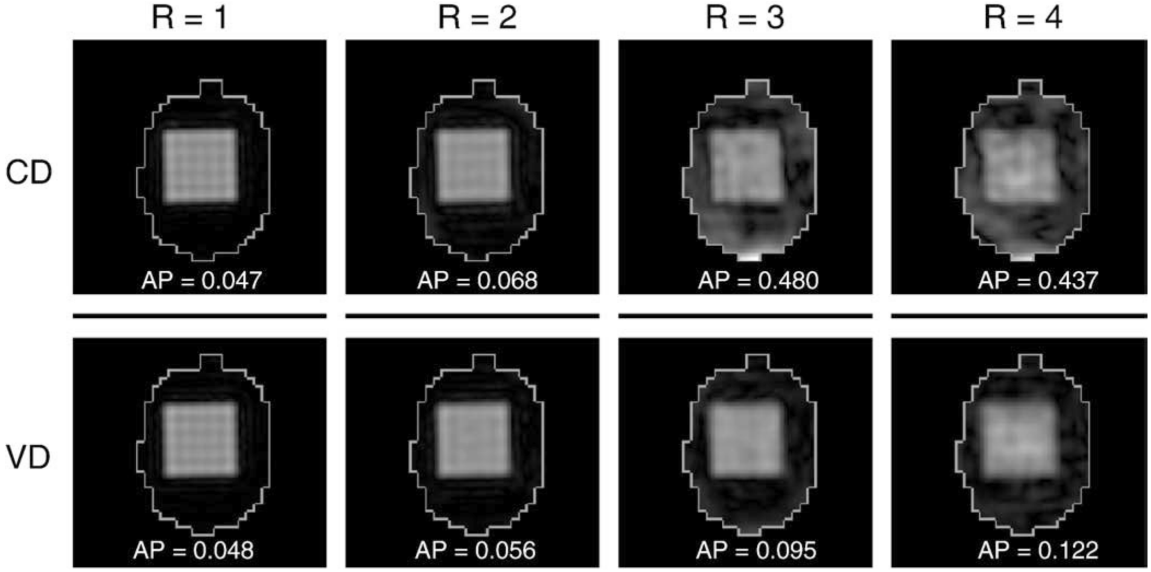

Figure 4.6. Excited patterns in Simulation I using (top) a CD spiral and (bottom) a VD spiral (α=2). In this experiment, a 9x9 cm^2 square pattern was excited using a four-channel transmit head coil. Columns from left to right: (1) R=1; (2) R=2; (3) R=3; (4) R=4. All the excitation patterns were masked with a head shape. The excitation AP is shown in each graph. With the same pulse duration, VD spirals resulted in patterns with reduced artifacts, although the resolution of the patterns was slightly compromised.

Figure 4.7 compares the RF waveforms of the four transmit channels. The magnitudes of the peak RF pulse were greatly reduced with the VD spiral.

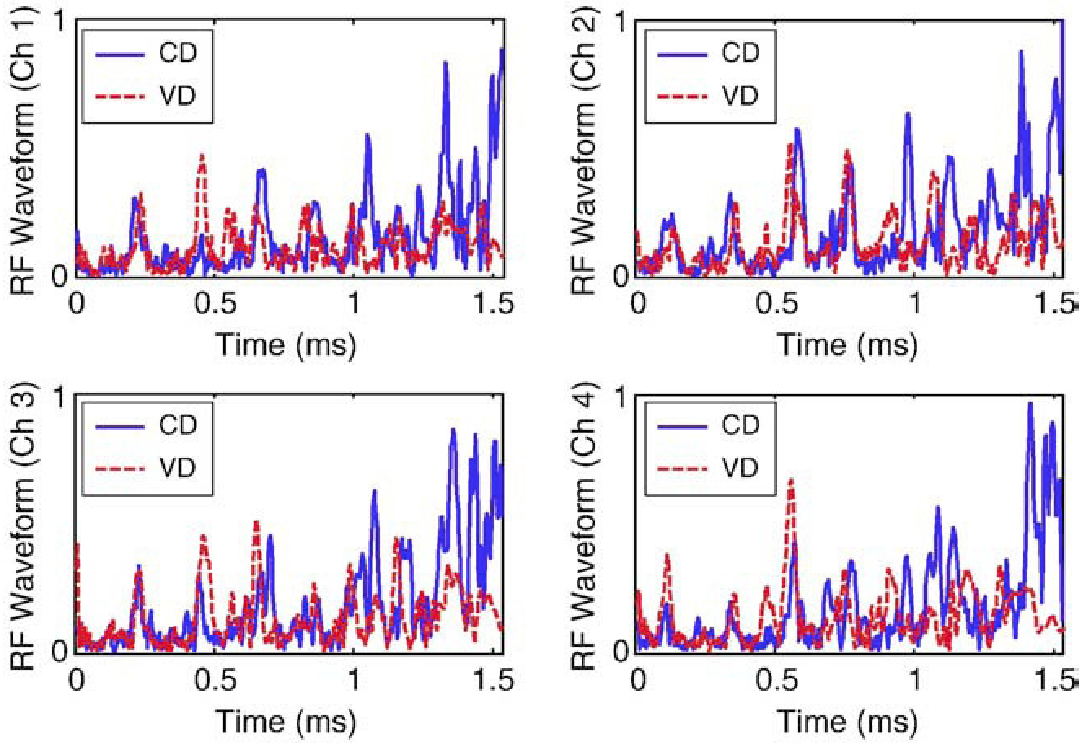

Figure 4.7. The RF waveforms of the four transmit channels. Note the reduced peak RF pulse magnitudes with the VD spiral in each channel.

Figure 4.8 compares the phase of RF waveforms from the CD spiral and the VD spirals for R = 2. One observation is that for VD spirals, the phase fluctuation seems to be mild comparing to CD spirals especially toward the k-space center.

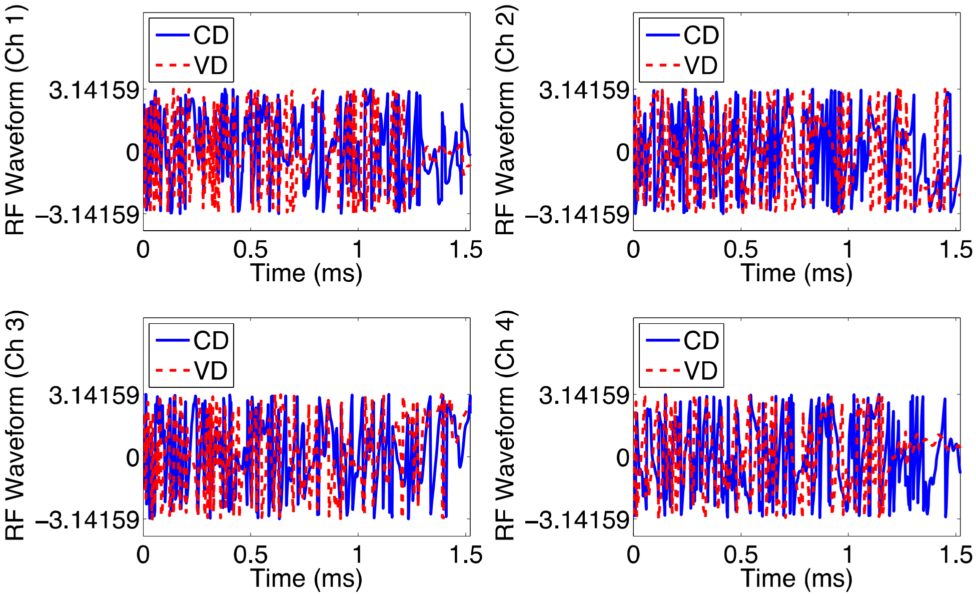

Figure 4.8. The phase of RF waveforms of the four transmit channels. Note the more mild phase fluctuation of the CD spirals especially towards the k-space center.

Figure 4.9 shows the SAR maps of five representative slices (out of 134 slices) of the brain with the CD spiral (α=1) and the VD spiral (α=2) for R=2. The VD spiral led to significantly reduced average SAR (about 50% at R=2) as compared with the CD spiral in this simulation.

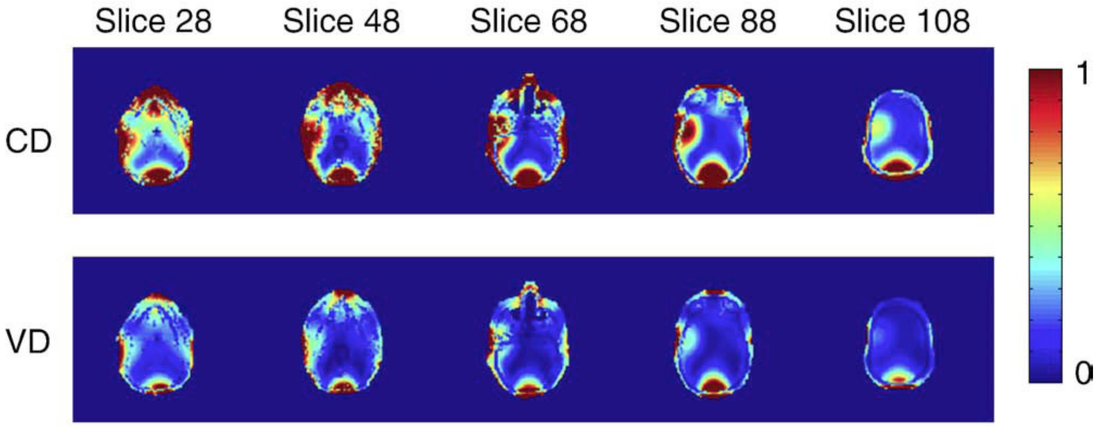

Figure 4.9. The SAR maps at six slice locations (out of 134 total slices) in Simulation I: (top) from the CD spiral and (bottom) from the VD spiral. The SAR maps are shown in the log scale after normalization for better visualization.

Simulation II

Figure 4.10 shows the excited small pattern with *R*=1, 2, 3 and 4. With the VD spiral (α=2), there was slight but noticeable loss of resolution, but the excitation AP was reduced.

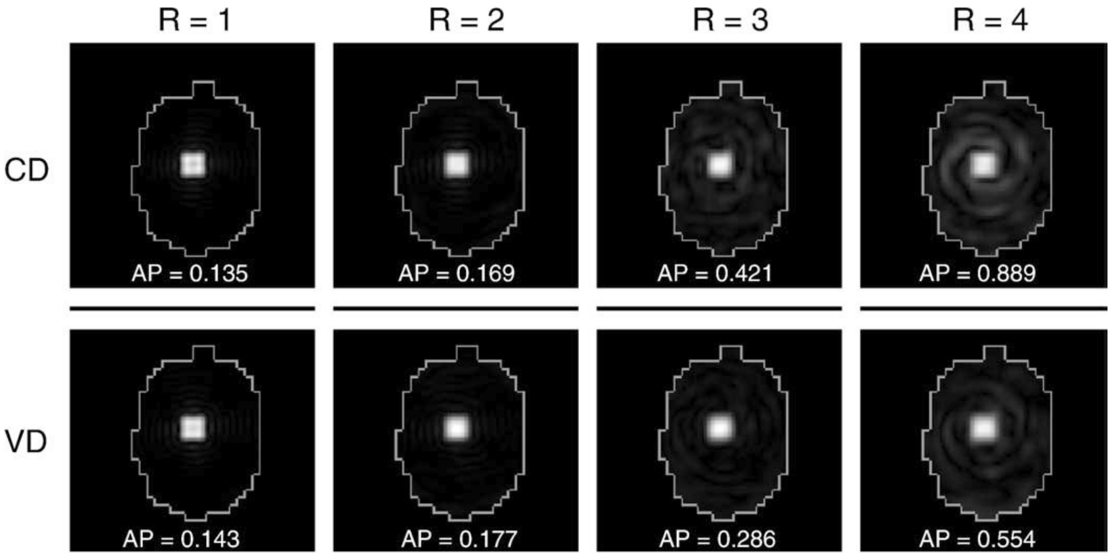

Figure 4.10. Excited patterns in Simulation II using (top) a CD spiral and (bottom) a VD spiral. In this experiment, a 3x3cm^2 square pattern was excited using a four-channel transmit head coil. Columns from left to right: (1) *R*=1; (2) *R*=2; (3) *R*=3; (4) *R*=4. All the excitation patterns were masked with a head shape. The excitation artifact power (AP) is shown in each graph. With the same pulse duration, VD spirals resulted in patterns with less AP, although the resolution of the patterns was slightly compromised.

Simulation III

Figure 4.11 shows the phase maps generated from parallel excitation with the CD spiral and the VD spiral (α=2) for a reduction factor of 2, where the two spirals have the same pulse duration. As shown, the VD spiral resulted in a slightly better phase map (using the desirable phase map shown in Fig. 4.4(C) as gold standard). This improvement is also reflected in the quantitative pErr computed for each case.

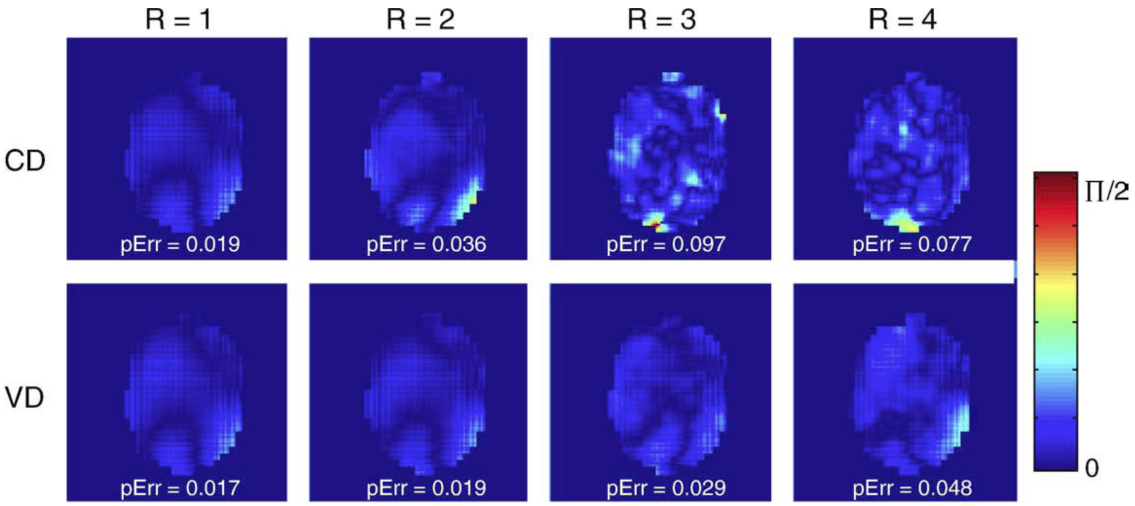

Figure 4.11. Phase Error (pErr) maps generated in the middle slice of the head model in Simulation III with the CD spiral and the VD spiral. Both spirals have the same pulse durations and average tip angles. Both excitation patterns were masked with a head shape. pErr is shown in each graph. The VD spiral resulted in better quality.

Figure 4.12 shows the SAR behavior for different acceleration factors (*R*=1, 2, 3 and 4) in the three simulations, in which the same small-tip angles were incorporated. All of the displayed curves were normalized by the average SAR corresponding to the CD spiral with *R*=4 in Simulation III. Several interesting observations can be made from this figure. (a) The average SAR increases with the acceleration factor R, which agrees with the results reported in Katscher et al. (10). (b) The average SAR decreases as the excitation k-space density increases at the center (from α=1 to 2, 3 and 4). (c) SAR reduction by using VD spirals is more significant for the large pattern (Simulation I: *R*=1, 70–80%; *R*=2, 40–50%; *R*=3, 10–15%; *R*=4, 20–30%) and the slow-varying phase map

(Simulation III: *R*=1, 50–60%; *R*=2, 20–30%; *R*=3, 5–10%, *R*=4, 8–10%) than for the small pattern (Simulation II: *R*=1, 80–90%; *R*=2, 60–80%; *R*=3, 30–40%; *R*=4, 40–50%). This last point is important. It indicates that it is particularly advantageous to use VD spirals for desired excitation patterns with concentrated k-space energy. For such patterns, the SAR reduction, by using the VD spiral (α=2, 3 and 4), can be 50%, as compared to the CD spiral. (d) Interestingly, among the three scenarios, the SAR is largest in Simulation III, which is discussed further below.

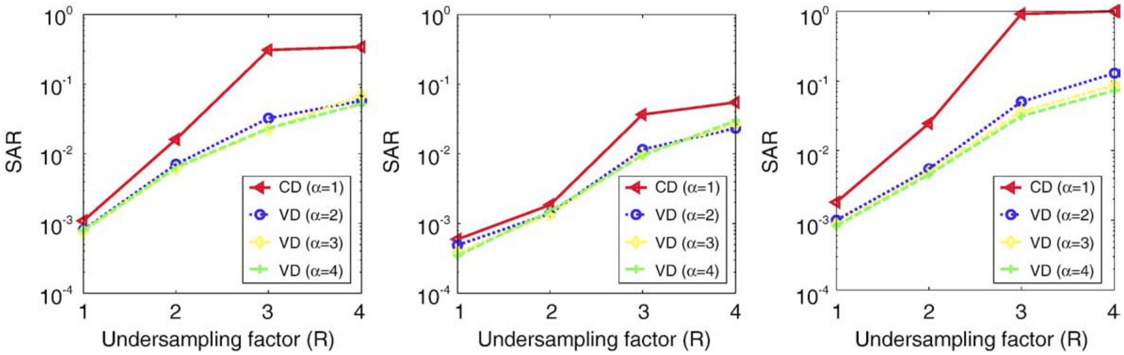

Figure 4.12. The SAR behaviors in three simulations for (left) the 9x9 cm^2 square excitation pattern (Simulation I); (middle) the 3x3 cm^2 square excitation pattern (Simulation II) and (right) a slow-varying phase map (Simulation III). In each case, the average SAR was computed as the spatially and temporally averaged value. Using VD spiral trajectories significantly reduced the SAR.

4.6 Discussion

Parallel excitation is an emerging technique that has the potential to address a number of problems in high-field MRI. Primary considerations in parallel excitation are the elevated RF power deposition (measured by SAR) and the spatial definition (resolution and artifacts). We have developed a parallel-excitation method using VD spirals to achieve reduced SAR with very little degradation in spatial resolution. By modeling a four-channel transmit system and a head model with the FDTD method, we were able to quantitatively evaluate the SAR distribution in accelerated parallel excitations. The results have demonstrated that, with the same pulse duration, proper use of VD spirals can significantly lower the SAR and can reduce the excitation artifacts in parallel excitation. These benefits come with a slight reduction in the spatial resolution of the excitation patterns. This resolution loss could be reduced by optimizing the excitation trajectory (38) or by using longer pulses (36). However, for fixed pulse duration, there is a tradeoff between resolution loss and SAR reduction. Further design optimization will be part of our future work. The method presented in this section differs from the method based on VERSE (33,39,43) in two aspects: (a) the VERSE methods lower SAR by adjusting the slew rate in CD trajectories, while our method adjusts slew rate on a VD trajectory (i.e., it allows adjustments of both the radial density and the angular density); and (b) there are residual artifacts coming from the inability of parallel excitation to completely compensate for the undersampling effect in the excitation k-space. Dense sampling in the excitation k-space center reduces the undersampling effect in this area where most RF energy is concentrated, thus generally reducing the AP.

Although we have shown results only for a small-tip angle excitation (e.g., a tip angle of 5° was used in our simulations), a similar SAR reduction has been observed for large-tip-angle excitations in our preliminary studies. The excitation artifacts were more complicated in large-tip-angle excitations, however, and further study is required in order to draw general conclusions. The simulations in the article were performed for 4.7 T because it is the field strength of the current animal scanner in our laboratory. However, the technique is expected to be useful in higher fields (e.g., 7 T) where SAR is potentially a more severe problem. In our simulation, the maximal SAR in Simulation I for R = 4 was approximately 11 W/kg using the CD spiral, which exceeded the FDA limit even at 4.7 T with the parameters used in our simulation. In this case, the proposed VD method can be used to reduce SAR for high reduction factors (e.g., R = 3 and 4). As the SAR rises quadratically with frequency (10,25), by scaling the SAR values according to the curve in Fig. 4.12 at 7 T, we expect that the SAR with the VD method using the parameters in this article could still be under the FDA limit for low reduction factors. However, for high reduction factors or larger flip angles, using the VD method alone would not sufficiently reduce the SAR. In these cases, longer RF pulse durations have to be used.

In addition, Figure 4.12 shows that, for a large excitation pattern (Simulations I and III) where more energy is concentrated in the k-space center, VD spirals are more effective in reducing SAR. This result indicates that, as makes intuitive sense, the optimal VD parameters will likely depend on the energy distribution of the desired excitation pattern. Notably, the SAR in Simulation III, the broadest pattern considered, was highest among the three. A possible explanation is that, in Simulation III, the whole FOV is excited with the same flip angle, but in Simulations I and II, only partial FOV (e.g., a square region) is excited. According to Parseval's theorem, the spectrum power of the excitation pattern is higher, and more power is required. The broader pattern localizes the power density in k-space center, enabling the greatest advantage from VD spirals.

Our study also verified several points that have been reported previously. For example, in parallel excitation, the SAR increases with increasing RF pulse duration reduction factors (i.e., with shortened pulses). In addition, the choice of excitation k-space trajectory (e.g., using different density parameters) can affect the excitation quality and SAR.

This study illustrates that significant gains in SAR performance can be made even with relatively straightforward k-space trajectory modification — a result that could be important as high-field magnets (e.g., 7.0 T) become more common. As a complement and further step to this study, the next section will focus on optimizing k-space trajectories and pulse design for reduced SAR.

5. RF PULSE DESIGN INCORPORATING TISSUE DIELECTRIC PROPERTIES IN PARALLEL EXCITATION

As discussed in Section 3, the application of parallel excitation is constrained by SAR in several ways. First, when high acceleration factors are used to shorten the RF pulses, SAR will dramatically increase because of the shortened pulse durations (10,44). Secondly, at high fields, this problem becomes even more serious because SAR can increase quadratically with the static field strength (10,18). Thirdly, in parallel excitation, the interacting effect of electric field and tissue dielectric properties and superimposed fields from all channels can create complex localized ”hot spots” (20,29), which makes SAR more difficult to study for individual subject (24).

Many recent studies have been focusing on addressing these issues. One method attempts to reduce maximum local SAR based on channel-dependent Tikhonov parameters (29). This method is based on the assumption that the coil-element closest to the maximum local SAR location contributes the most to the corresponding hot spot. Other existing methods have been focused on directly or indirectly reducing the SAR by minimizing the RF power used in the excitation pulses, either by exploiting the extra freedom in parallel excitation pulse design, by using variable-density k-space trajectory (34), or by minimizing a cost function that incorporates both excitation error and the RF power (39,45), or by jointly optimizing both RF pulses and the excitation k-space trajectory (32-33,46). These methods have shown to be very efficient; however they do not directly minimize the RF heating effect on the tissue, i.e., SAR. In fact, due to the lack of accessibility of tissue property for each specific patient, SAR is not convenient to predict in practice. Even when measuring tissue properties while the patient is in the scanner is possible (47), it may be inefficient in terms of total imaging time.

In this section, we propose an algorithm to adjust the conventional pulse sequences in order to directly reduce SAR for parallel excitation. The method is an extension of (43). A unique feature in this algorithm is that it could also incorporate tissue dielectric properties and densities from human models (48) or from real-time measurement (47). The pulse design problem is formulated in a Lagrange optimization framework where the excitation k-space is adjusted to achieve much lower SAR for the given tissue properties. Subsequently, the RF pulses are computed based on the adjusted excitation k-space. Computer simulations of a 4-channel transmit system are used to verify the new method to achieve 2-dimensional (2-D) parallel excitations. The results show that the proposed method can achieve significant SAR reductions, by taking tissue properties into consideration, without enlonging the pulse duration.

5.1 Joint RF Pulse and K-space Trajectory Adjustment

The proposed algorithm starts with the conventional parallel excitation RF pulse design method described in Section 3 using a k-space trajectory. Then, the gradient waveforms and RF pulses are adjusted to reduce SAR while preserving the pulse duration and excitation pattern. Tissue dielectric properties and densities are incorporated in the process in order to reduce SAR. The workflow of the proposed method is shown in Fig. 5.1.

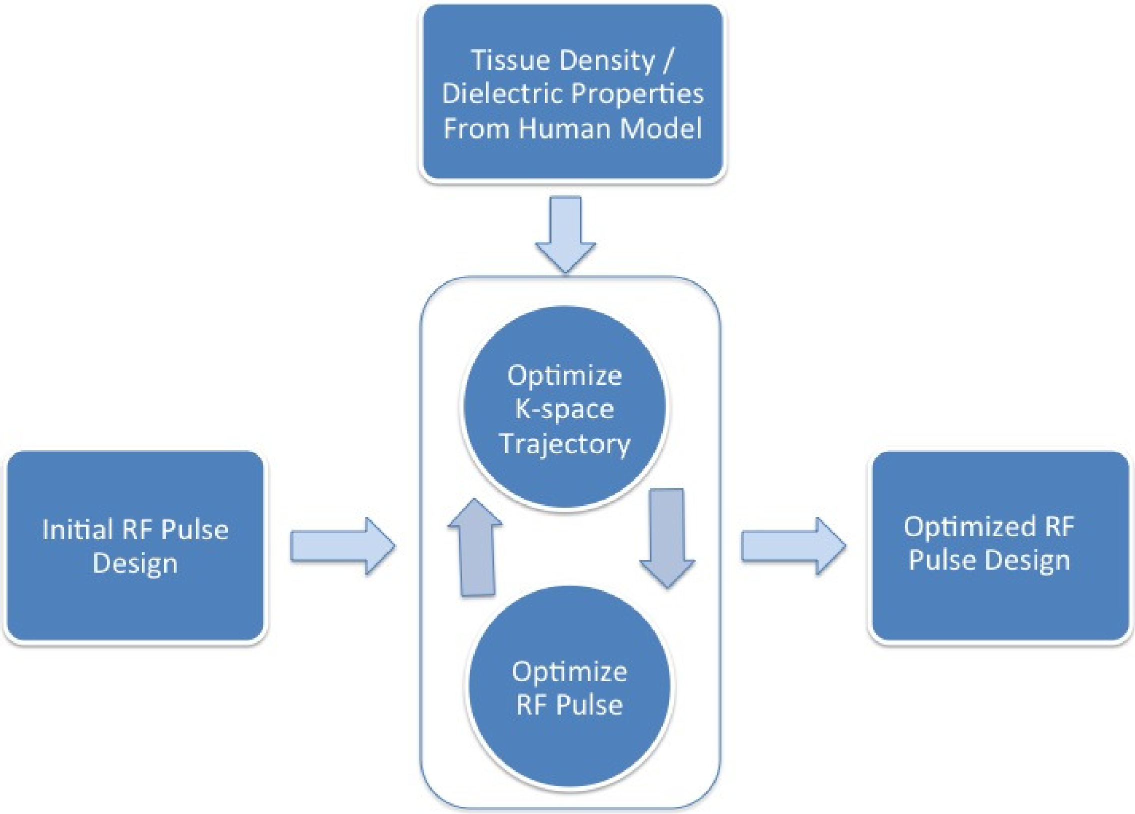

Figure 5.1. Flow chart of the proposed method.

In this process, the k-space trajectory will be iteratively updated until it achieves minimum SAR and satisfies both the gradient magnitude and slew rate limit. In doing so, the gradient magnitude and the gradient slew rate must operate with the hardware limit (the gradient magnitude limit will control how broad the trajectory could go in the k-space during a certain time; and the gradient slew rate limit will control how fast the gradient could change). The proposed method is developed based on similar mathematical principal of (43). Specifically, define

$\mathbf{G}(q)=G_x(q)+iG_y(q)$: the initial gradient at time point q

$\mathbf{B}_{1,l}(q)=B_{1,x}(q)+iB_{1,y}(q)$: the initial RF pulses from the l-th channel at time point q

$\Delta t(q)$: the initial time interval at time point q

$\mathbf{G}_{new}(q)=G_{new,x}(q)+iG_{new,y}(q)$: the new gradient at time point q

$\mathbf{B}_{new}(q)=B_{new,x}(q)+iB_{new,y}(q)$: the new RF pulses from the l-th channel at time point q

$\Delta t_{new}(q)$: the new time interval at time point q

Under the small-flip angle assumption and that the pulse duration T is short enough that the relaxation effect can be ignored, the magnetization using original pulse sequence after time T can be obtained from the Bloch equation

$$\mathbf{M}(\mathbf{r},T)=\mathbf{M}_0\sum_{l=1}^{L}S_l(\mathbf{r})\prod_{q=1}^{Q}\exp\left(\begin{bmatrix} 0 & \mathbf{G}(q)\mathbf{r} & -B_{1,y}(q) \\ -\mathbf{G}(q)\mathbf{r} & 0 & B_{1,x}(q) \\ -B_{1,y}(q) & B_{1,x}(q) & 0 \end{bmatrix} i\gamma\Delta t\right) \tag{5.1}$$

The $\prod_{q=1}^{Q}\exp(\cdot)$ terms in Eq. (5.1) represent a sequence of small rotations of the magnetization. From Eq. (5.1), it is easy to see that if two RF pulses yield the same magnetization rotation at each step, then the final magnetization will be the same.

Therefore, in order to achieve the same final excitation pattern, the initial and the new pulse sequences are constrained to satisfy

$$\begin{cases} \mathbf{G}_{new}(q)\Delta t_{new}(q) = \mathbf{G}(q)\Delta t(q) \\ \mathbf{B}_{1new,l}(q)\Delta t_{new}(q) = \mathbf{G}_{1,l}(q)\Delta t(q) \end{cases} \tag{5.2}$$

The new pulse sequence should have the same pulse duration as the original one. Therefore,

$$\textstyle\sum_{q=1}^{Q}\Delta t_{new}(q) = \sum_{q=1}^{Q}\Delta t(q) \tag{5.3}$$

After incorporating Eq. (5.2), this equation can be rewritten as

$$\sum_{q=1}^{Q}\left[\mathbf{G}(q)/\mathbf{G}_{new}(q) - 1\right]\Delta t(q) = 0 \tag{5.4}$$

The design goal is to find a set of new gradient and RF waveforms to yield reduced SAR while keeping the same pulse duration. In the proposed design method, SAR is evaluated as the time-space-averaged value over the pulse duration using the formula provided in (5,10). Specifically, the SAR within a region-of-interest (ROI) can be expressed as

$$SAR = \frac{1}{P}\sum_{p=1}^{P}\left\{\frac{\sigma(\mathbf{r}_p)}{2\rho(\mathbf{r}_p)}\frac{1}{T}\sum_{q=1}^{Q}\left|\mathbf{E}_{tot}(\mathbf{r}_p,q)\right|^2\Delta t_{new}(q)\right\} \tag{5.5}$$

where σ denotes tissue conductivity, ρ is tissue density, and P is the total number of spatial points within the ROI, Q is the total number of time points. $\mathbf{E}_{tot}$ is the total electric field, which is proportional to the sum of the RF waveforms weighted by the 3D electric field sensitivity.

$$\left|\mathbf{E}_{tot}\left(\mathbf{r}_p, q\right)\right|^2 \propto \left(\left|\sum\nolimits_{l=1}^{L} \mathbf{E}_{l,x}\left(\mathbf{r}_p\right)\mathbf{B}_{1new,l}\left(q\right)\right|^2 + \left|\sum\nolimits_{l=1}^{L} \mathbf{E}_{l,y}\left(\mathbf{r}_p\right)\mathbf{B}_{1new,l}\left(q\right)\right|^2 + \left|\sum\nolimits_{l=1}^{L} \mathbf{E}_{l,z}\left(\mathbf{r}_p\right)\mathbf{B}_{1new,l}\left(q\right)\right|^2\right)$$

where $\mathbf{E}_{l,x}$, $\mathbf{E}_{l,y}$ and $\mathbf{E}_{l,z}$ are the electric-field sensitivity along x, y, z direction of the l-th channel. After incorporating Eqs (5.2) and (5.3), it can be shown that

$$\begin{aligned}
SAR = {} & \frac{1}{P}\sum_{p=1}^{P}\left\{\frac{\sigma\left(\mathbf{r}_p\right)}{2\rho\left(\mathbf{r}_p\right)}\frac{1}{T} \bullet \right. \\
& \left. \sum_{q=1}^{Q}\left(\left|\sum\nolimits_{l=1}^{L}\mathbf{E}_{l,x}\left(\mathbf{r}_p\right)B_{1new,l}(q)\right|^2 + \left|\sum\nolimits_{l=1}^{L}\mathbf{E}_{l,y}\left(\mathbf{r}_p\right)B_{1new,l}(q)\right|^2 + \left|\sum\nolimits_{l=1}^{L}\mathbf{E}_{l,z}\left(\mathbf{r}_p\right)B_{1new,l}(q)\right|^2\right)\Delta t_{new}(q)\right\} \\
\propto {} & \sum_{p=1}^{P}\left\{\frac{\sigma\left(\mathbf{r}_p\right)}{2\rho\left(\mathbf{r}_p\right)}\frac{1}{T}\sum_{q=1}^{Q}\left(\left|\sum\nolimits_{l=1}^{L}\mathbf{E}_{l,x}\left(\mathbf{r}_p\right)B_{1,l}(q)\right|^2 + \left|\sum\nolimits_{l=1}^{L}\mathbf{E}_{l,y}\left(\mathbf{r}_p\right)B_{1,l}(q)\right|^2 + \left|\sum\nolimits_{l=1}^{L}\mathbf{E}_{l,z}\left(\mathbf{r}_p\right)B_{1,l}(q)\right|^2\right)\frac{\Delta t(q)^2}{\Delta t_{new}(q)}\right\} \\
= {} & \sum_{p=1}^{P}\left\{\frac{\sigma\left(\mathbf{r}_p\right)}{2\rho\left(\mathbf{r}_p\right)}\frac{1}{T}\sum_{q=1}^{Q}\left(\left|\sum\nolimits_{l=1}^{L}\mathbf{E}_{l,x}\left(\mathbf{r}_p\right)B_{1,l}(q)\right|^2 + \left|\sum\nolimits_{l=1}^{L}\mathbf{E}_{l,y}\left(\mathbf{r}_p\right)B_{1,l}(q)\right|^2 + \left|\sum\nolimits_{l=1}^{L}\mathbf{E}_{l,z}\left(\mathbf{r}_p\right)B_{1,l}(q)\right|^2\right)\frac{B_{new}(q)\Delta t(q)}{B(q)}\right\} \\
= {} & \sum_{p=1}^{P}\left[\frac{\sigma\left(\mathbf{r}_p\right)}{2\rho\left(\mathbf{r}_p\right)}\frac{1}{T}\sum_{q=1}^{Q}\left(\mathbf{EB}\left(\mathbf{r}_p, q\right)\frac{G_{new}(q)\Delta t(q)}{G(q)}\right)\right] \\
= {} & \sum_{q=1}^{Q}\left(\sum_{p=1}^{P}\left(\frac{\sigma\left(\mathbf{r}_p\right)}{2\rho\left(\mathbf{r}_p\right)}\mathbf{EB}\left(\mathbf{r}_p, q\right)\right)\frac{G_{new}(q)}{G(q)}\Delta t(q)\right)
\end{aligned}$$

Thus

$$SAR \propto \sum\nolimits_{q=1}^{Q}\left(\sum\nolimits_{p=1}^{P}\frac{\sigma\left(\mathbf{r}_p\right)}{2\rho\left(\mathbf{r}_p\right)}\mathbf{EB}\left(\mathbf{r}_p, q\right)\frac{\mathbf{G}_{new}(q)}{\mathbf{G}(q)}\Delta t(q)\right) \tag{5.6}$$

where

$$\mathbf{EB}\left(\mathbf{r}_p, q\right) = \left|\sum\nolimits_{l=1}^{L}\mathbf{E}_{l,x}\left(\mathbf{r}_p\right)\mathbf{B}_{1new,l}(q)\right|^2 + \left|\sum\nolimits_{l=1}^{L}\mathbf{E}_{l,y}\left(\mathbf{r}_p\right)\mathbf{B}_{1new,l}(q)\right|^2 + \left|\sum\nolimits_{l=1}^{L}\mathbf{E}_{l,z}\left(\mathbf{r}_p\right)\mathbf{B}_{1new,l}(q)\right|^2 \tag{5.7}$$

Thus, the optimal gradient waveform to minimize SAR is

$$\operatorname{argmin}_{\mathbf{g}_{new}} \sum\nolimits_{q=1}^{Q}\sum\nolimits_{p=1}^{P}\left(\frac{\sigma\left(\mathbf{r}_p\right)}{2\rho\left(\mathbf{r}_p\right)}\mathbf{EB}\left(\mathbf{r}_p, q\right)\frac{\mathbf{G}_{new}(q)}{\mathbf{G}(q)}\right)\Delta t(q) \tag{5.8}$$

subject to Eq. (5.4) and maximum gradient constraint

$$\mathbf{G}_{new}(q) < \mathbf{G}_{\max} \tag{5.9}$$

This optimization problem can be reformulated as minimizing the Lagrange function:

$$L(g_{new}, \lambda) = \sum_{q=1}^{Q} \left\{ \sum_{p=1}^{P} \left[\frac{\sigma(\mathbf{r}_p)}{2\rho(\mathbf{r}_p)} \mathbf{EB}(\mathbf{r}_p, q) \frac{\mathbf{G}_{new}(q)}{\mathbf{G}(q)} \Delta t(q) \right] + \lambda_q \left(\frac{\mathbf{G}(q)}{\mathbf{G}_{new}(q)} - 1 \right) \right\} \tag{5.10}$$

where λ_q are Lagrange multipliers (49). Since this problem is separable, minimizing $L(\mathbf{G}_{new}, \lambda)$ over time is equivalent to minimizing $l(\mathbf{G}_{new}(q), \lambda_q)$ for each time interval, which is

$$l(\mathbf{G}_{new}(q), \lambda_q) = \sum_{p=1}^{P} \left[\frac{\sigma(\mathbf{r}_p)}{2\rho(\mathbf{r}_p)} \mathbf{EB}(\mathbf{r}_p, q) \frac{\mathbf{G}_{new}(q)}{\mathbf{G}(q)} \Delta t(q) \right] + \lambda_q \left(\frac{\mathbf{G}(q)}{\mathbf{G}_{new}(q)} - 1 \right) \tag{5.11}$$

To do so, we set the derivative of the function with respect to the gradient $\mathbf{G}_{new}(q)$ to be equal to zero and find the solution as

$$\mathbf{G}_{new}^2(q) = c \frac{\mathbf{G}^2(q)}{\sum_{p=1}^{P} \frac{\sigma(\mathbf{r}_p)}{2\rho(\mathbf{r}_p)} \mathbf{EB}(\mathbf{r}_p, q) \Delta t(q)} \tag{5.12}$$

where the constant *c* is solved iteratively until both constraints Eq. (5.4) and Eq. (5.9) are satisfied.

In summary, the design procedure is as follows.

1) Design an initial pulse $\{\mathbf{G}(q), \mathbf{B}(q), \Delta t(q)\}$ using methods in Section 3 for a specified excitation pattern.

2) Solving initial value of $\mathbf{G}_{new}^{(1)}(q)$ and $c^{(1)}$ using Eq.(5.2) and Eq.(5.12).

3) Solving $\mathbf{B}_{new}^{(1)}(q)$ and $\Delta t_{new}^{(1)}(q)$ using Eq.(5.2)

4) Check the gradient slew rate. If it exceeds the maximum gradient slew rate, set it to be $\mathbf{GS}_{\max}$. Then update $\mathbf{G}_{new}^{(1)}(q)$

5) Check each $\mathbf{G}_{new}^{(1)}(q)$. If it exceeds the gradient constraint, set it to be $\mathbf{G}_{\max}$.

6) Use Eq. (5.4) to calculate $c^{(2)}$ for the rest of gradient.

7) Repeat the step 2) to 5) and update with the new gradient $\mathbf{G}_{new}(q)$ until all $\mathbf{G}_{new}(q)$ satisfy the maximum gradient constraint and Eq.(5.12).

The process normally takes only several iterations to reach the convergence. Once the gradient waveform is determined, the RF waveforms can be calculated using the standard procedure as described in the previous section.

5.2 Tissue Dielectric Properties Mapping

In the proposed design procedure, the tissue dielectric properties and densities are incorporated in the SAR definition. Means to measure or estimate these parameters are readily available. For example, human models have been developed and categorized into large man/woman, medium man/woman, small man/woman, pregnant woman, infants, etc., which have been used widely for SAR related simulations (44,48). There is also method available for measuring dielectric properties in real-time (47). Thus, the proposed algorithm will be flexible to be either application-oriented or to be patient-specific.

1) Application-oriented design with estimated tissue properties from human models

For application-oriented group studies, such brain imaging, the tissue properties can be estimated by roughly choosing the appropriate human model from various human model libraries (48) and EM softwares, like xFDTD or HFSS. Then the model could be be registered to the patient's size using maturely developed image registration algorithms (50-52). The preprocessing can be done offline and will not require online tissue property measurement.

2) Patient-specific design with measured tissue properties

For patient-specific individual studies, a more accurate measurement of tissue properties can be derived from the spatial sensitivity distributions of the applied RF coils (47). This provides more accurate models for SAR minimization but would require additional imaging time to measure the tissue properties.

5.3 Results

To test the proposed method, a four-channel transmit coil and a 3D head model with known dielectric properties and tissue density were modeled at 4.7 Tesla (200 MHz) using xFDTD 6.3 bio-pro software package (Remcom Inc. State College, PA). This simulation was the same as in our previous study (53) and in Section 4 of this dissertation. Ideal RF current sources at 200 MHz were used as feeding source for coil decoupling (40). The xFDTD output gave the steady state 3D E fields and B fields produced by constant current excitations. The electromagnetic fields at a mid-axial slice of the head were used for the 2D pulse design. The SAR was evaluated over the whole head. More details of the simulation can be found in (34).

All parallel excitation and optimization algorithms were implemented using Matlab (The Mathworks, Inc, Natick, MA) on a 2.53 GHz Intel Core 2 Duo Mac Pro laptop of 4 GB memory. Three simulations are performed using three different excitation patterns respectively.

In the first simulation (Simulation I), the parallel excitation aims to achieve B1+ homogeneity within a circular region of interest (ROI) of the head in the center slice. Figure 5.2(a) shows the B1+ field inhomogeneity of the four-channel transmit head coil. Figure 5.2(b) shows the circular ROI with a radius of 5 cm. In this simulation, the desirable excitation pattern is the one that will complement the B1+ inhomogeneity in Fig. 5.2(a) to achieve a uniform excitation within the ROI in Figure 5.2(b).

In the second simulation (Simulation II), the parallel excitation aims to compensate B0 inhomogeneities within a circular ROI. Figure 5.2(c) shows the B0 field inhomogeneity. The circular ROI is the same as in Simulation I (Fig. 5.2(b)). The desirable excitation pattern is the one that would complement the B0 inhomogeneity in Fig. 5.2(c) to achieve a uniform excitation within the ROI in Fig. 5.2(b).

In the third simulation (Simulation III), parallel excitation aims to excite a uniform circular region with a radius of 12 cm as shown in Fig. 5.2(d). The purpose is to compare SAR resulted from RF pulses designed with / without incorporating tissue density and dielectric properties.

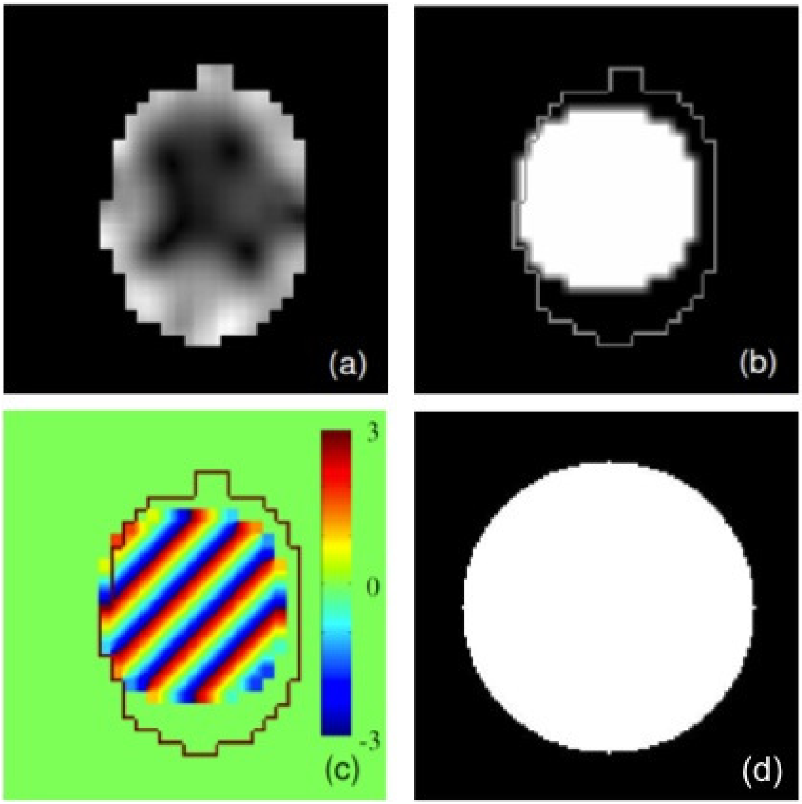

Figure 5.2. Field inhomogeneity patterns and desirable excitation patterns used in the three simulations. (a) B1+ field inhomogeneity pattern within the head region (Simulation I); (b) Desirable circular excitation pattern (Simulation I and Simulation II); (c) B0 field inhomogeneity within the head region (in radians) (Simulation II); (d) Desirable circular excitation pattern (Simulation III).

For all simulations for 2D excitation pattern, the FOV was set to 32 cm, which was discretized over a 64x64 grid. The initial excitation trajectory was an EPI. When designing both the conventional EPI trajectory and the adjusted k-space trajectory, maximum gradient and gradient slew rate were 5 gauss/cm and 15 gauss/cm/ms respectively. The k-space trajectories were designed to achieve a field of excitation (FOX) of 16 cm, 8 cm and 5.3 cm respectively, which corresponds to an acceleration factor R = 2, 4 and 6 in terms of pulse duration using the parallel excitation. A Bloch simulator was used to verify the excited patterns (http://www-mrsrl.stanford.edu/). The artifact power (AP) was used to evaluate the accuracy of the excitation pattern. It was calculated as the normalized mean square error (34) over the ROIs as shown in Fig. 5.2.

Figure 5.3 shows the excitation trajectories of conventional EPI (dashed lines), and optimized EPI (solid lines) from the proposed method in the two scenarios: Fig. 5.3(a) corresponds to Simulation I; and Fig. 5.3(b) corresponds to Simulation II. In both Fig. 5.3(a) and Fig. 5.3(b), FOX was 8 cm (R = 4). The k-space trajectories are overlaid on top of the k-space spectrum of the desirable excitation patterns. Comparing the conventional and the optimized trajectories, one can observe that the optimized trajectory is more dense in the region where k-space energy is more concentrated, i.e., k = 0 in Fig. 5.3 (a). The k-space trajectory progressed from uniform EPI to be denser in the k-space center. More interestingly, as shown in Fig. 5.3(b), when the k-space spectrum distribution shifted (due to the phase modulation in Simulation II), the optimized k-space trajectory was automatically adjusted accordingly. This shows that the proposed algorithm can automatically adapt to the desirable excitation pattern to achieve reduced SAR, as dense sampling in the high-energy area of the excitation k-space tend to lower SAR, as observed in several previous literatures (32,34,43).

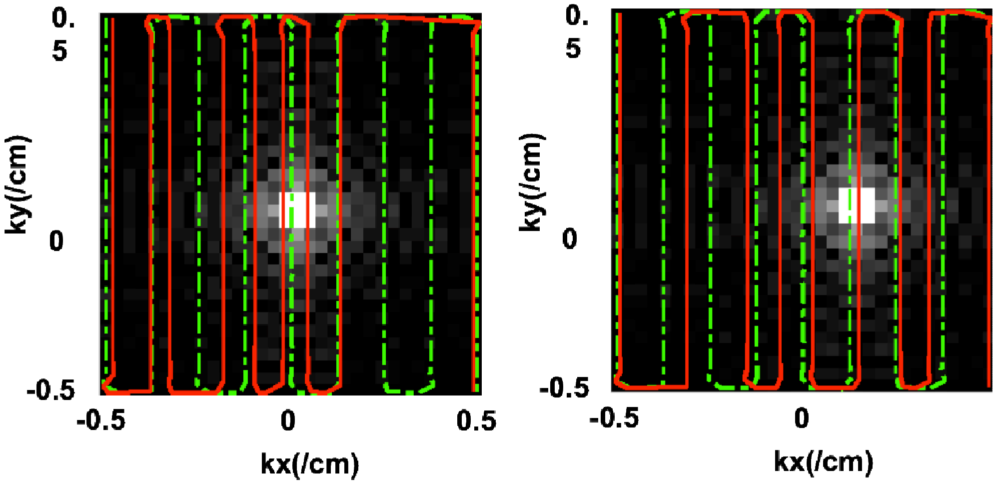

Figure 5.3. Excitation k-space trajectories from the optimized k-space trajectory (solid red lines) and the conventional EPI (dashed green lines) overlaid on the energy spectrum of the desirable excitation patterns. (a) in Simulation I and (b) in Simulation II. The results illustrate that the proposed method can automatically adjust the gradients according to the desirable excitation patterns.

Figure 5.4 shows the excitation patterns using the conventional method and the proposed method in Simulation I for R = 2. The AP values are listed below the patterns. Figure 5.4 (a-c) shows the excitation patterns using the conventional method, corresponding to R = 2, 4 and 6. Figure 5.4 (d-f) shows the corresponding excitation patterns using the proposed method. Only the patterns inside the head mask are shown. For both methods, the excitation patterns are similar, and the results from the proposed method show slightly improved accuracy (i.e., smaller AP). Therefore, the proposed method significantly reduced SAR while maintained the fidelity of the excitation pattern.

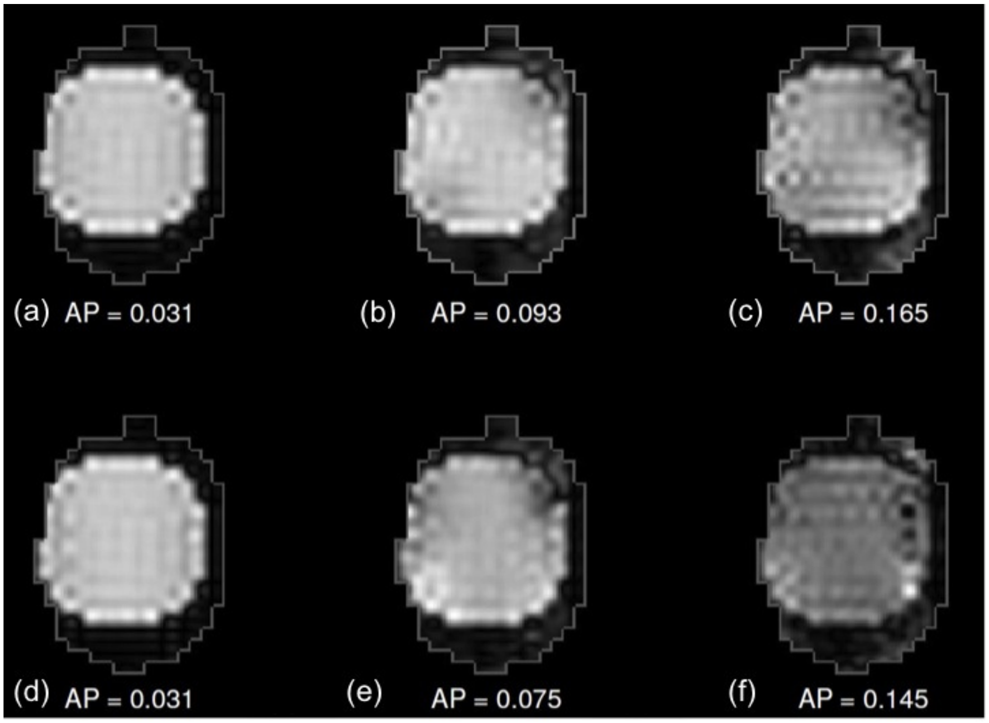

Figure 5.4. Excited patterns in Simulation I using (a-c) a conventional method and (d-e) the proposed method. Columns from left to right: (1) R = 2; (2) R = 4, and (3) R = 6. All excitation patterns were masked with a head contour. The normalized excitation artifact power (AP) (34) is shown in each graph.

Figure 5.5 compares the SAR distribution using conventional method and proposed method in Simulation II. Five slices out of 134 slices in the head are shown. With acceleration factor $R = 4$, using conventional design, there are obvious hot spots near the boundary of the brain. Using optimized EPI design, the SAR in the hot spot regions were significantly reduced.

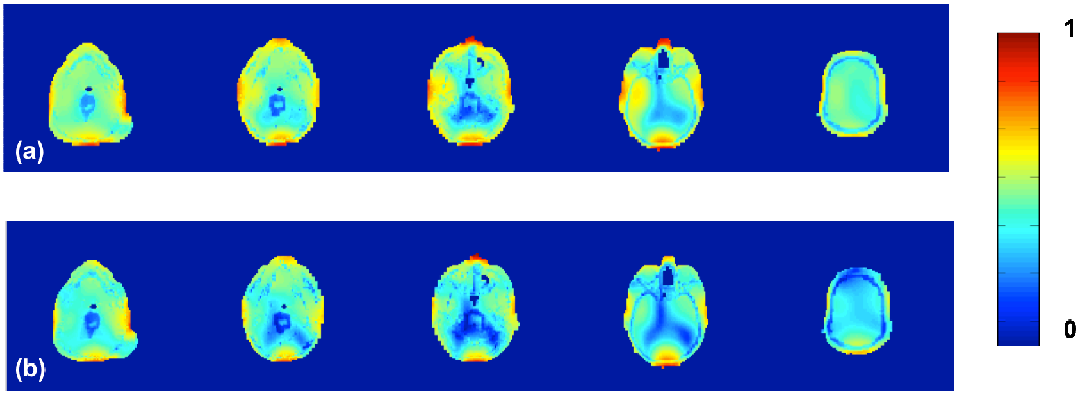

Figure 5.5. The SAR maps at 5 slice locations (out of 134 total slices) in Simulation II. (Top) using conventional method with standard EPI trajectory, and (Bottom) using the proposed design method. The SAR maps are shown in the dB after normalization for better visualization. Note that the hot spots were significantly reduced by using the proposed method.

In order to show the overall SAR behavior as the acceleration factor increases, Figure 5.6 summaries the averaged SAR for different acceleration factor (R = 2, 4 and 6) in Simulation I and II. For each plot, the SAR value is normalized by the averaged SAR value of conventional method at R = 6. With the conventional design, the SAR increases dramatically as acceleration factor increases. However, with the proposed design method, the SARs are significantly lower. It is observed that at low acceleration factors, the improvement of adjusted EPI over conventional EPI is less dramatic. However, at high acceleration factors, such as $R = 6$, the proposed method can achieve about 60-70% SAR reduction comparing to the conventional design.

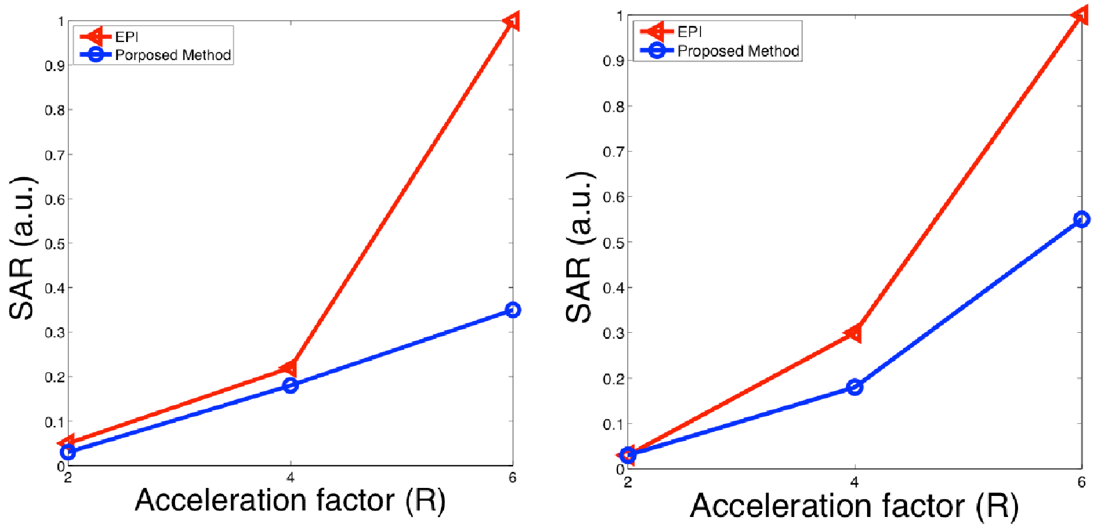

Figure 5.6. SAR v.s. acceleration factor in the simulated parallel excitation experiments I and II. (a) for B1 field inhomogeneity compensation (Simulation I); (b) for B0 field inhomogeneity compensation (Simulation II). In each case, the average SAR was computed as the spatially and temporally averaged value over the ROI, which is a radius-5 cm circle at the center of the brain.

Figure 5.7 shows SAR maps generated from simulation III using three method: the conventional method, the proposed method without incorporating tissue properties; and the proposed method incorporating tissue dielectric properties, all for an acceleration factor $R = 4$. As shown, the proposed method can reduce SAR even without known tissue properties (i.e., assuming uniform tissues). Most noticeably, when the tissue properties are considered in the design, further SAR reduction was achieved: the global mean SAR in (b) was by a factor of 1.3 as compared to (a), which was further reduced by a factor of 3 in (c).

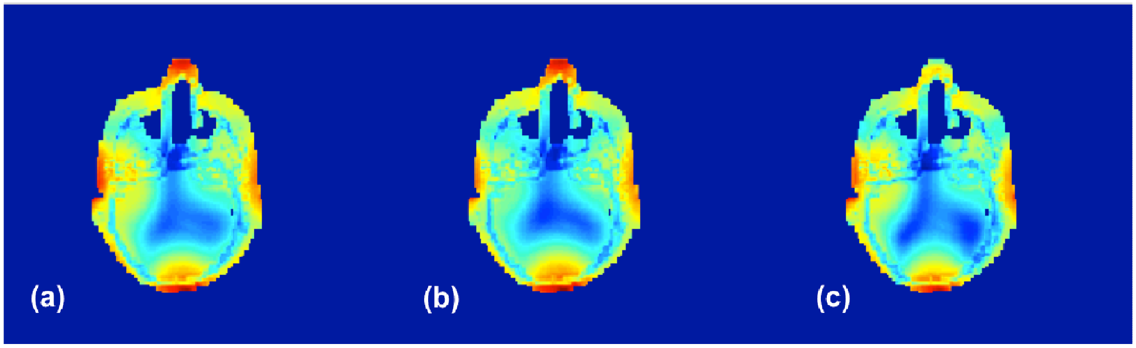

Figure 5.7. SAR maps of center axial brain slice in Simulation III using: (a) the conventional method; (b) the proposed method without incorporating tissue dielectric properties; (c) the proposed method incorporating tissue dielectric properties. The results are for acceleration factor $R = 4$.

5.4 Discussion

In parallel excitation, RF power deposition is a critical issue, particularly at high magnetic fields. In this section, an iterative design method was presented herein for designing the multi-channel RF pulses and gradient waveforms. Computer simulations have shown that the proposed method can significantly reduce the SAR without sacrificing the excitation quality or increasing the pulse duration. In addition, although the proposed method can directly lower the SAR as compared with conventional design methods, incorporating tissue dielectric properties can further reduce SAR.

There are three major findings in this study. First, the results show that the new method can design parallel excitation RF pulses sequences with significantly reduced SAR.

The second finding is the new design method is able to automatically adapt the k-space trajectory to the spectrum of the excitation patterns. In this simulation, we choose rectilinear k-space trajectory to demonstrate the effectiveness of the algorithm. However, it is also applicable with other trajectories, such as spiral (34,37), and spokes (54).

The third finding is that tissue density and dielectric properties are important for

RF pulses design with the purpose of optimizing SAR. SAR is the combined product of RF pulse, tissue properties, and electrical field. Our results show that ignoring tissue properties in parallel excitation RF pulses design, may compromise the SAR performance.

The proposed method requires some extra computation time for pulse design, but the additional computation is still tractable. In many cases, the optimization can be done offline and will not affect real-time imaging. The simulations are in 2D in this manuscript, but this method can also be extended to 3D, once a trajectory is chosen. The proposed method can be used to optimize for both local SAR and spatially averaged SAR. One potential problem of using the method is that in the optimization step, information of tissue density and dielectric properties are required in order to evaluate SAR and to calculate the new gradient. This information is usually not available during a clinic scanning, or may require extra scanning to acquire. As a simplification, such information can either be acquired from registering certain similar human model to match the scanned subject size (51-52). These human models are available from various libraries or EM softwares, like xFDTD or HFSS. In certain cases, when only RF power matters, this method can also be converted to a RF power optimization by simply replace the SAR calculation in Eq. (5.5) with RF power calculation by removing the $\sigma(\mathbf{r})$ and the $\rho(\mathbf{r})$ terms.

6. CONCLUSION AND FUTURE WORKS

Parallel excitation is a promising technique that can address several problems in MRI, particularly at high fields. Unfortunately, literatures have shown that reduced RF pulse duration and field interaction among multiple transmit coils may cause elevated RF power deposition, or SAR, in parallel excitation, which hinders its clinical applications (10-11).

To address this problem, two new RF pulse design methods for parallel excitation were developed in this dissertation.

First, we have developed a parallel-excitation method using variable-density spirals to achieve reduced SAR with very little degradation in spatial resolution. By modeling a four-channel transmit system and a head model with xFDTD, we were able to quantitatively evaluate the SAR distribution in the human head in parallel excitations. The results have demonstrated that, with the same pulse duration, proper use of VD spirals can significantly lower the SAR and can reduce the excitation artifacts in parallel excitation. These benefits come with a slight reduction in the spatial resolution of the excitation patterns.

Second, an iterative design method was developed for designing the multi-channel RF pulses and gradient waveforms. Computer simulations have shown that the proposed method can significantly reduce SAR without sacrificing the excitation quality or increasing the pulse duration. In addition, although the proposed method can directly lower the SAR as compared with conventional design methods, incorporating tissue dielectric properties can further reduce SAR.

For future directions, experiments will need to be performed to verify the performance of the proposed RF pulse design methods and evaluate SAR. There are four major components needed to be taken care of for carrying out the experiments.

This first key component is availability of parallel transmission systems, including MRI scanners which support multi-channel RF pulse transmission and multi-channel transmit coil arrays which could independently drive RF waveforms simultaneously. Katscher and Zhu (5,7) presented the first experimental results for parallel excitation. In both studies, the parallel RF transmissions were mimicked through a series of single-channel RF transmission. However, these experiment design were based on the linearity of small flip angle excitation(55), and so would not be suitable for large flip angle excitation. More recently, many research groups have investigated the development of parallel transmit coil arrays (6,40,56-58). The technology advancement in parallel transmit coil design have made experimental verification possible at various field strength, such as 3T, 4.7T, 7T etc.

The second key component is RF pulse sequence programming onto the MRI scanner. For one thing, each MRI scanner is equipped with gradient systems that are constrained by maximum gradient and maximum slew rate. The duration of maximum gradient is also constrained by duty cycle for SAR management. Thus, Before actual experiments, pilot simulation studies, such as the simulations described in Section 4 and 5, need to be performed to make sure the desired gradients and RF waveform don't violate the hardware specification. For another, care must be taken so that RF pulse programming is compatible with the software platform version in the scanner.

The third key component is SAR evaluation. Measuring SAR is not a trivial task, which requires information of electrical field, tissue density and dielectric properties. These are all difficult to measure in real time (59). Currently, a common approach to estimate SAR is to simulate the coil array's electromagnetic fields using human models in software like xFDTD, Remcom and calculate SAR distribution based on these field simulations (44,60-61). Several alternative approaches to evaluate SAR indirectly include detecting the temperature changes using temperature probes (62), infrared cameras (63) or MR temperature mapping (64). On a recent publication (65), a Power Prediction and Monitoring (PPM) method was proposed for SAR monitoring. In this model, forward and reflected power on the transmit channels were measured using power sensors. This method is promising to be integrated into PRESCAN for SAR prediction, but it still requires prior information of tissue density and dielectric properties. On the other hand, Katscher et.al has published a paper on determining electric conductivity and local SAR via B1 maping (47). Integration of these methods may provide possibility to measure electrical field and tissue dielectric properties in real time, and thus monitor SAR in real time.

REFERENCES

1. Pauly J, Nishimura D, Macovski A. A k-space analysis of small-tip-angle excitation. J Magn Reson 1989;81:43-56.
2. Webb AG, Collins CM, Versluis MJ, Kan HE, Smith NB. MRI and localized proton spectroscopy in human leg muscle at 7 Tesla using longitudinal traveling waves. Magn Reson Med 2010;63:297-302.
3. Vega-Vazquez M, Cobas JC, Martin-Pastor M. Fast multidimensional localized parallel NMR spectroscopy for the analysis of samples. Magn Reson Chem 2010;48:749-752.
4. Bornert P, Schaffter T. Curved slice imaging. Magn Reson Med 1996;36:932-939.
5. Zhu Y. Parallel excitation with an array of transmit coils. Magn Reson Med 2004;51:775-784.
6. Setsompop K, Wald LL, Alagappan V, Gagoski B, Hebrank F, Fontius U, Schmitt F, Adalsteinsson E. Parallel RF transmission with eight channels at 3 Tesla. Magn Reson Med 2006;56:1163-1171.
7. Katscher U, Bornert P, Leussler C, van den Brink JS. Transmit SENSE. Magn Reson Med 2003;49:144-150.
8. Grissom W, Yip CY, Zhang Z, Stenger VA, Fessler JA, Noll DC. Spatial domain method for the design of RF pulses in multicoil parallel excitation. Magn Reson Med 2006;56:620-629.

9. Zelinski AC, Angelone LM, Goyal VK, Bonmassar G, Adalsteinsson E, Wald LL. Specific absorption rate studies of the parallel transmission of inner-volume excitations at 7T. J Magn Reson Imaging 2008;28:1005-1018.

10. Katscher U, Vernickel P, Overweg J. Basics of RF power behaviour in parallel transmission. In: Proceedings of the International Society for Magnetic Resonance in Medicine. Miami, USA; 2005. p 17.

11. Graesslin I, Glaesel D, Biederer S, Schweser F, Vernickel P, Bornert P, Annighoefer B, Stahl H, Dingemans H, Mens G, Harvey P, Katscher U. SAR in Parallel Transmission. PIERS Online 2008;4:681-685.

12. Wilm BJ, Svensson J, Henning A, Pruessmann KP, Boesiger P, Kollias SS. Reduced field-of-view MRI using outer volume suppression for spinal cord diffusion imaging. Magn Reson Med 2007;57:625-630.

13. Smith TB, Nayak KS. Reduced field of view MRI with rapid, B(1) -robust outer volume suppression. Magn Reson Med 2012;67:1316-1323.

14. Kessler H, Mronga S, Gemmecker G. Multi-dimensional NMR experiments using selective pulses. Magn Reson Chem 1991;29:527-557.

15. Boulant N, Cloos MA, Amadon A. B1 and B0 inhomogeneity mitigation in the human brain at 7 T with selective pulses by using average Hamiltonian theory. Magn Reson Med 2011;65:680-691.

16. Yang C, Deng W, Alagappan V, Wald LL, Stenger VA. Four-dimensional spectral-spatial RF pulses for simultaneous correction of B1+ inhomogeneity and susceptibility artifacts in T2*-weighted MRI. Magn Reson Med 2010;64:1-8.

17. Pruessmann KP, Weiger M, Scheidegger MB, Boesiger P. SENSE: sensitivity encoding for fast MRI. Magn Reson Med 1999;42:952-962.

18. Katscher U, Bornert P, van den Brink JS. Theoretical and numerical aspects of transmit SENSE. IEEE Trans Med Imaging 2004;23:520-525.

19. Groetsch CW. The theory of Tikhonov regularization for Fredholm equations of the first kind. Boston: Pitman Publishing Program; 1984.

20. Katscher U, Rohrs J, Bornert P. Basic considerations on the impact of the coil array on the performance of Transmit SENSE. MAGMA 2005;18:81-88.

21. Shellock FG. Radiofrequency energy-induced heating during MR procedures: a review. J Magn Reson Imaging 2000;12:30-36.

22. Schaefer DJ. Safety aspects of radiofrequency power deposition in magnetic resonance. Magn Reson Imaging Clin N Am 1998;6:775-789.

23. Shellock F. Magnetic Resonance Procedures: Health Effects and Safety. Los Angeles: CRC Press; 2000.

24. IEC Standard 60601–2-33. Particular requirements for the safety of magnetic resonance equipment for medical diagnosis. Chicago: International Electrotechnical Commission; 2004.

25. Schick F. Whole body MRI at high field: technical limits and clinical potential. Eur Radiol 2005;15:946-959.

26. Zelinski AC, Goyal VK, Angelone LM, Bonmassar G, Wald LL, Adalsteinsson E. Designing RF pulses with optimal specific absorption rate (SAR) characteristics and exploring excitation fidelity, SAR and pulse duration tradeoffs. In:

Proceedings of the International Society for Magnetic Resonance in Medicine. Berlin, Germany; 2007. p 1699.

27. Gabriel S, Lau RW, Gabriel C. The dielectric properties of biological tissues: II. Measurements in the frequency range 10 Hz to 20 GHz. Phys Med Biol 1996;41:2251-2269.

28. Yang QX, Wang J, Collins CM, Smith MB, Zhang X, Ugurbil K, Chen W. Phantom design method for high-field MRI human systems. Magn Reson Med 2004;52:1016-1020.

29. Cloos MA, Luong M, Ferrand G, Amadon A, Le Bihan D, Boulant N. Local SAR reduction in parallel excitation based on channel-dependent Tikhonov parameters. J Magn Reson Imaging 2010;32:1209-1216.

30. Wang Z, Oh S, Smith M, Collins C. RF shimming considering both excitation homogeneity and SAR. In: Proceedings of the International Society for Magnetic Resonance in Medicine. Berlin, Germany; 2007. p 1022.

31. Ullmann P, Wuebbeler G, Junge S, Seifert F, Ruhm W, Hennig J. SAR-Analysis for Transmit SENSE with a 4-Channel Head Array at 3 T. In: Proceedings of the International Society for Magnetic Resonance in Medicine. Seattle, USA; 2006. p 601.

32. Yip CY, Grissom WA, Fessler JA, Noll DC. Joint design of trajectory and RF pulses for parallel excitation. Magn Reson Med 2007;58:598-604.

33. Wu X, Akgun C, Vaughan JT, Andersen P, Strupp J, Ugurbil K, Van de Moortele PF. Adapted RF pulse design for SAR reduction in parallel excitation with experimental verification at 9.4 T. J Magn Reson 2010;205:161-170.

34. Liu Y, Feng K, McDougall MP, Wright SM, Ji J. Reducing SAR in parallel excitation using variable-density spirals: a simulation-based study. Magn Reson Imaging 2008;26:1122-1132.

35. Yip CY, Fessler JA, Noll DC. Iterative RF pulse design for multidimensional, small-tip-angle selective excitation. Magn Reson Med 2005;54:908-917.

36. Schroder C, Bornert P, Aldefeld B. Spatial excitation using variable-density spiral trajectories. J Magn Reson Imaging 2003;18:136-141.

37. Kim DH, Adalsteinsson E, Spielman DM. Simple analytic variable density spiral design. Magn Reson Med 2003;50:214-219.

38. Stenger VA, Boada FE, Noll DC. Variable-density spiral 3D tailored RF pulses. Magn Reson Med 2003;50:1100-1106.

39. Xu D, King KF, Liang ZP. Variable slew-rate spiral design: theory and application to peak B(1) amplitude reduction in 2D RF pulse design. Magn Reson Med 2007;58:835-842.

40. Kurpad K, Wright SM, Boskamp E. RF current element design for independent control of current amplitude and phase in transmit phased Arrays. Concepts in Magn Reson part B: Magn Reson Eng 2006;29B:75-83.

41. Sutton BP, Noll DC, Fessler JA. Fast, iterative image reconstruction for MRI in the presence of field inhomogeneities. IEEE Trans Med Imaging 2003;22:178-188.

42. Ullmann P, Junge S, Wick M, Seifert F, Ruhm W, Hennig J. Experimental analysis of parallel excitation using dedicated coil setups and simultaneous RF transmission on multiple channels. Magn Reson Med 2005;54:994-1001.

43. Conolly SM, Nishimura D, Macovski A. Variable-rate selective excitation. J Magn Reson 1988;78:440-458.

44. Massire A, Cloos MA, Luong M, Amadon A, Vignaud A, Wiggins CJ, Boulant N. Thermal simulations in the human head for high field MRI using parallel transmission. J Magn Reson Imaging 2012.

45. Deniz CM, Alon L, Brown R, Sodickson DK, Zhu Y. Specific absorption rate benefits of including measured electric field interactions in parallel excitation pulse design. Magn Reson Med 2012;67:164-174.

46. Ma C, Xu D, King KF, Liang ZP. Joint design of spoke trajectories and RF pulses for parallel excitation. Magn Reson Med 2011;65:973-985.

47. Katscher U, Voigt T, Findeklee C, Vernickel P, Nehrke K, Dossel O. Determination of electric conductivity and local SAR via B1 mapping. IEEE Trans Med Imaging 2009;28:1365-1374.

48. Collins CM, Smith MB. Signal-to-noise ratio and absorbed power as functions of main magnetic field strength, and definition of "90 degrees " RF pulse for the head in the birdcage coil. Magn Reson Med 2001;45:684-691.

49. Boyd S, Vandenberghe L. Convex Optimization: Cambridge University Press; 2004.

50. West JB, Fitzpatrick JM, Toms SA, Maurer CR, Jr., Maciunas RJ. Fiducial point placement and the accuracy of point-based, rigid body registration. Neurosurgery 2001;48:810-817.

51. Ji J, Jiraraksopakun Y. Model-based simulation of dynamic magnetic resonance imaging signals. Biomedical Signal Processing and Control 2008;3:305-311.

52. Fitzpatrick JM, West JB, Maurer CR, Jr. Predicting error in rigid-body point-based registration. IEEE Trans Med Imaging 1998;17:694-702.

53. Liu Y, Ji J. Minimal-SAR RF pulse optimization for parallel transmission in MRI. Annual International Conference of the IEEE Engineering in Medicine and Biology Society. Vancouver, Canada; 2008. p 5774.

54. Setsompop K, Wald LL, Alagappan V, Gagoski BA, Adalsteinsson E. Magnitude least squares optimization for parallel radio frequency excitation design demonstrated at 7 Tesla with eight channels. Magn Reson Med 2008;59:908-915.

55. Bornert P, Aldefeld B. On spatially selective RF excitation and its analogy with spiral MR image acquisition. MAGMA 1998;7:166-178.

56. Zhu Y, Giaquinto R, Watkins R, Kerr A, Pauly J, Vogel M, Piel J, Foo T, Hancu I, Park K. Transmit coil array for accelerating 2D excitation on an eight-channel parallel transmit system In: Proceedings of the International Society for Magnetic Resonance in Medicine. Seattle, USA; 2006. p 122.

57. Hollingsworth N, Moody K, Nielsen J, Noll DC, McDougall MP, Wright SM. An Easily Integrated Eight Channel Parallel Transmit System for Transmit SENSE

Applications. In: Proceedings of the International Society for Magnetic Resonance in Medicine. Montreal, Canada; 2011. p 3832.

58. Adriany G, Auerbach EJ, Snyder CJ, Gozubuyuk A, Moeller S, Ritter J, Van de Moortele PF, Vaughan T, Ugurbil K. A 32-channel lattice transmission line array for parallel transmit and receive MRI at 7 tesla. Magn Reson Med 2010;63:1478-1485.

59. Ullmann P. Multiple-Channel RF Pulses and SAR Control. Proceedings of the International Society for Magnetic Resonance in Medicine. Hawaii; 2008. p 38.

60. Graesslin I, Biederer S, Falaggis K, Vernickel P, Dingemans H, Mens G, Roeschmann P, Leussler C, Zhai Z, Morich M, Katscher U. Real-time SAR Monitoring to ensure Patient Safety for Parallel Transmission Systems. In: Proceedings of the International Society for Magnetic Resonance in Medicine. Berlin, Germany; 2007. p 1086.

61. Collins CM. Numerical field calculations considering the human subject for engineering and safety assurance in MRI. NMR Biomed 2009;22:919-926.

62. Shrivastava D, Schlentz B, Kulesa J, Snyder C, DelaBarre L, Hanson T, Iaizzo P, Vaughan J. RF safety at 9.4T - porcine in vivo results. In: Proceedings of the International Society for Magnetic Resonance in Medicine. Berlin, Germany; 2007. p 1087.

63. Ibrahim TS, Lee R. Evaluation of MRI RF probes utilizing infrared sensors. IEEE Trans Biomed Eng 2006;53:963-967.

64. Ishihara Y, Calderon A, Watanabe H, Okamoto K, Suzuki Y, Kuroda K, Suzuki Y. A precise and fast temperature mapping using water proton chemical shift. Magn Reson Med 1995;34:814-823.

65. Zhu Y, Alon L, Deniz CM, Brown R, Sodickson DK. System and SAR characterization in parallel RF transmission. Magn Reson Med 2012;67:1367-1378.

VITA

Yinan Liu received the B.S. degree in electrical engineering from University of Science and Technology of China in 2004 and her PhD degree in electrical engineering at Texas A&M University, College Station. She has interned and worked at Microsoft, MD Anderson Cancer Center, GE Healthcare and Department of Veteran Affairs Medical Center. Her current research interests include digital signal processing and medical imaging.